PHYSICAL REVIEW MATERIALS **8**, 043401 (2024)

Incomplete monolayer regime and mixed regime of nanowire growth

Frank Glas[*]
Université Paris-Saclay, CNRS, Centre de Nanosciences et de Nanotechnologies, 10 bd. Thomas Gobert, 91120 Palaiseau, France

(Received 21 November 2023; revised 21 February 2024; accepted 13 March 2024; published 1 April 2024)

We study theoretically the nucleation and development of sequences of monolayers during the vapor-liquid-solid growth of semiconductor nanowires, in the case where all material originates from the catalyst nanodroplet. If at nucleation the droplet content is insufficient, a fractional monolayer forms quickly before propagating more slowly; the droplet then refills during a random waiting time until next nucleation. We compare the proper incomplete monolayer regime, where this occurs for each monolayer, with the mixed regime where full or fractional monolayers may form, depending on the nucleation event. We investigate in detail the most general case of the mixed regime at arbitrary temperature. Under simple assumptions of the dependence of nucleation and desorption rates upon liquid state, valid at least for III-V compounds (with low concentration of the volatile group V atoms in the liquid), we calculate semi-analytically the probability density of the concentration at nucleation and the statistics of the propagation, waiting and monolayer cycle times, without any growth simulation and duly accounting for the correlations between successive monolayers. We find that an effective incomplete monolayer regime, whereby a huge fraction of nucleations produce incomplete monolayers, may prevail over a wide range of nanowire-droplet geometry and growth conditions, with complete monolayers becoming frequent only at large nanowire radius, input rate, and temperature. We explain why, in this regime, growth tends to become quasideterministic, with a very narrow distribution of monolayer cycle times, which is beneficial for a precise control of nanowire ensembles and heterostructures. We investigate quantitatively the case of self-catalyzed GaAs nanowires and discuss the extension of our conclusions to other systems.

DOI: 10.1103/PhysRevMaterials.8.043401

I. INTRODUCTION

Various growth modes of semiconductor nanowires (NWs) have now been observed at atomic resolution in real time *in situ* transmission electron microscopy (TEM) experiments [1–9]. This has confirmed that vapor-liquid-solid (VLS) growth usually involves the sequential nucleation and propagation of individual biatomic monolayers (MLs) at the interface between the NW stem and the liquid catalyst nanoparticle, as described by modern theories of NW growth [10–14].

In many VLS systems, at least one NW constituent is present at very low concentration in the liquid droplet. For III-V NWs, this is the case of the volatile P and As group V species, the concentration of which is on the order of a fraction of percent [8,15–17]. This concentration is so low that, due to the small size of the droplet and the variety of kinetic processes at play, it may vary significantly during the cycle of formation of each ML.

In particular, just after the nucleation of a new ML, the droplet is suddenly depleted from this element. Indeed, once a critical nucleus forms, the attachment of atoms to the new ML becomes energetically favorable. We could therefore expect the rapid formation of a full ML. However, since the droplet is a nanosize mother phase, the amount of a scarce NW constituent available at nucleation may even be insufficient for this. Recall that, in VLS growth, two main morphologies of the solid-liquid interface are observed, depending on the droplet contact angle. The interface can be truncated (with a solid wedge missing at its periphery) [2–4,7,18] or planar (with two terraces during ML growth). We consider the latter case, which prevails at intermediate contact angles and, in III-V NWs, usually produces the wurtzite (WZ) crystal phase [4,5,7,8]. The ML can then only grow from atoms provided by the liquid (as opposed to the deepening of the wedge, which is another source of material for the ML in case of truncation [19]).

Previously, we studied two extreme instances of the liquid depletion effect. Based on *ex situ* (postgrowth) TEM experiments [16], we first considered the case where there is *always* enough group V atoms to build quickly a whole ML after nucleation. We modeled this *complete ML (CML) regime* numerically [16] and analytically [20]. These calculations show that, as observed in our experiments, the distribution of the numbers of MLs formed during successive equal times may be sub-Poissonian, contrary to what would result from independent nucleation events. This is due to an anticorrelation in time of the nucleation events: because of droplet depletion, the chemical potential of a III-V pair in the droplet, and thus the nucleation probability, are less after a first nucleation event than just before. We called this effect *nucleation antibunching* [16].

To introduce the second extreme case of liquid depletion (Sec. II A), we note that it may, however, happen that there is not enough group V element in the droplet for a full ML to form quasi-instantaneously. Then, a fractional ML (i.e., a

---

[*] frank.glas@c2n.upsaclay.fr; https://www.c2n.universite-paris-saclay.fr

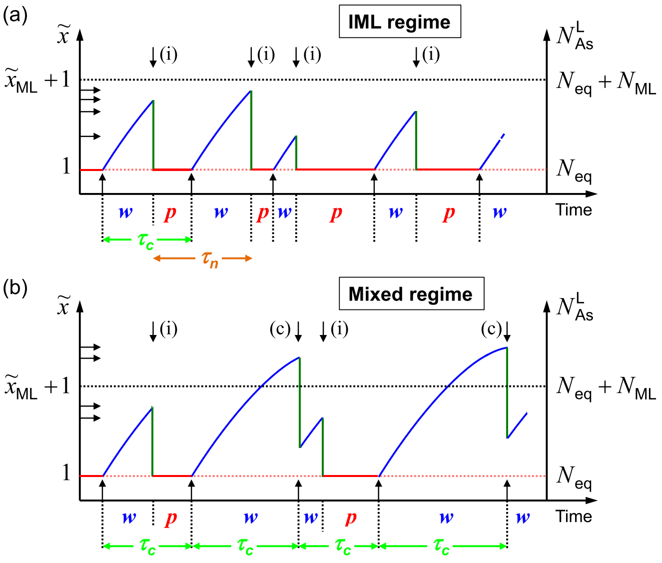

FIG. 1. Schematics of the formation of a sequence of 4 MLs in the (a) IML and (b) mixed regimes. The variation of the As content of the droplet, given in terms of number of atoms (right scale) and reduced concentration $\tilde{x} = x/x_{eq}$ (left scale), would become linear in absence of desorption from the liquid. Nucleation events and ML completions are marked by arrows pointing down and up, respectively, and the droplet contents at nucleation by horizontal arrows. There is enough As in the droplet at nucleation to form a whole ML at events (c), after which $p = 0$, and not enough at events (i). N_{ML}, $\tilde{x}_{ML}$: amount of As in a ML; N_{eq}: droplet content at equilibrium with solid GaAs. w: waiting time; p: propagation time; τ_c (τ_n): ML cycle time between completion (nucleation) of successive MLs.

ML occupying only part of the interface, given that all MLs, complete or not, have the same biatomic height) may form very quickly after nucleation, consuming all atoms available [events labeled (i) in Fig. 1]. Our theoretical work shows that, as a first approximation, the depleted liquid reaches equilibrium with the solid and remains in this state until ML completion [21]. During this ML *propagation time* p, all atoms provided by the vapor thus serve not to enrich the droplet but to extend the ML. After ML completion, the droplet can refill and liquid supersaturation builds up; this *waiting time* w ends with a new nucleation event (Fig. 1). From now on, we qualify such MLs as *incomplete*. The reset to equilibrium concentration, at which nucleation is forbidden, produces another type of nucleation anticorrelation. Being set by nucleation, the waiting time and the concentration at nucleation vary randomly between MLs. Even in the case of elementary semiconductors, where the atomic concentration in the liquid is rather large [22,23], the amount available above equilibrium may also be low and incomplete MLs might form at nucleation.

II. THE INCOMPLETE MONOLAYER AND MIXED REGIMES OF NANOWIRE GROWTH

A. The incomplete monolayer regime and quasideterministic growth

Apart from the CML regime, the second extreme case of liquid depletion that we already considered is when (for a given NW in given growth conditions) there is *never* enough group V element in the droplet to allow the ML to form quasi-instantaneously [Fig. 1(a)] [8,21]. Our *in situ* observations of narrow VLS-grown GaAs NWs are *a priori* compatible with this strict *incomplete monolayer (IML) regime*, as shown by the fact that $p > 0$ for all MLs [5,8].

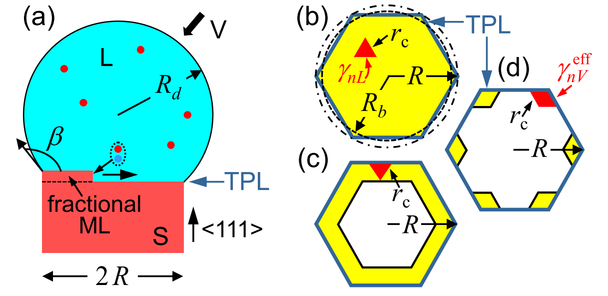

FIG. 2. Schematics of system geometry. R: NW radius; R_d, R_b, β: droplet radius, base radius, and contact angle; TPL: triple phase line. (a) Side view. Fractional solid (S) NW MLs of fixed height grow by step flow (horizontal arrow) via addition of III-V pairs from the liquid (L) refilled by the vapor (V). Top views of NW-liquid interface with areas Σ_n (in yellow) allowed for nucleation (b) on whole facet, (c) at TPL, or (d) at corner, and (b), (c) critical triangular or (d) rhomboidal nuclei of side r_c (in red). In panel (d), each corner nucleation locus has the same area as the nucleus.

In the following, we consider a single NW with fixed radius and droplet contact angle (neglecting the small changes due to intermittent consumption combined with steady refill [21]), growing at temperature T [Fig. 2(a)]. For sake of simplicity and in line with our previous work [8,17], we formulate the problem in terms of self-catalyzed GaAs NWs (Ga-As droplet), although our results apply to other materials and to catalyst droplets involving a foreign metal. If N^L_i is the instantaneous number of atoms of species i in the liquid, $N^L_{As} \ll N^L_{Ga}$ and the relative variations of N^L_{Ga} are negligible. When calculating the As atomic concentration $x = N^L_{As}/N^L_{tot} \ll 1$ (which fully defines the state of the binary liquid at given temperature), we thus consider the total number N^L_{tot} of atoms (Ga, As and possibly the foreign catalyst) in the droplet as constant and, for a given NW, we can reason indifferently in terms of N^L_{As} or x.

A striking property of the IML regime is that growth may become *self-regulated*, with each ML cycle lasting *exactly* the same time [8]. To understand why, let us assume growth conditions such that (A1) the IML regime is realized and (A2) group V desorption from the liquid is negligible, as occurs at relatively low temperature. The As concentration after waiting time w is $x(w) = x_{eq} + Fw$, where x_{eq} is the equilibrium concentration and F a constant describing the input of As in the droplet, depending on geometry and external flux. The linear time variation follows from assumption (A2) and the fact that $x = x_{eq}$ at $w = 0$ from assumption (A1), which guarantees that the liquid is at equilibrium during propagation of the previous ML. The fractional ML formed quickly after nucleation (bringing the liquid back to equilibrium) thus contains a number of As atoms corresponding to $x_{eq} + Fw - x_{eq} = Fw$. During ML propagation, the input Fp to the droplet is entirely used for ML growth (there is neither storage in the liquid nor desorption). At the end of propagation, exactly one ML has formed, hence $Fw + Fp = x_{\mathrm{ML}}$, with x_{ML} corresponding to 1 ML-worth of As in the droplet. Under these conditions, the ML cycle time $\tau_c = w + p$, measured between ML completions (Fig. 1), is thus the same, $\tau_c = x_{\mathrm{ML}}/F$, *whatever the ML*. This remarkable property is achieved although w varies between MLs due to the stochasticity of nucleation. It clearly results from a compensation between random waiting time and following propagation time. If w is long, a large ML fraction is formed right after nucleation, and the time p needed to complete it is short.

Conditions (A1) and (A2) must be met for this strictly deterministic growth regime to be realized. Assume for instance that (A1) holds, but not (A2). Then, after waiting time w, $x(w) = x_{\mathrm{eq}} + g(w)$, with g a certain sublinear function of time (since desorption increases with concentration). If desorption consumes fraction ζ of input at x_{eq}, then $g(w) + (1-\zeta)Fp = x_{\mathrm{ML}}$, which shows that τ_c varies between MLs, because w does. In the opposite case where (A2) is met, but not (A1), consider a complete ML that formed quickly after nucleation since there was enough As in the liquid [events (c) in Fig. 1(b)]. For this ML, $p = 0$ and the concentration after ML formation is some $x_0 > x_{\mathrm{eq}}$. Then, for the next ML, $x(w) = x_0 + Fw$, the fraction of ML formed at nucleation is $x_0 + Fw - x_{\mathrm{eq}}$, and $x_0 + Fw - x_{\mathrm{eq}} + Fp = x_{\mathrm{ML}}$. Therefore, $\tau_c = (x_{\mathrm{ML}} + x_{\mathrm{eq}} - x_0)/F$ varies between MLs since x_0 (which itself results from random nucleation at $x_0 + x_{\mathrm{ML}}$) has no reason to be the same after the fast formation of different complete MLs. We may also simply notice that, for these complete MLs, $p = 0$, hence $\tau_c = w$ with w random [Fig. 1(b)].

Note that, strictly speaking, assumptions (A1) and (A2) are incompatible: in absence of desorption, x increases linearly with time as long as there is no nucleation, and there is a probability that it will overcome $x_{\mathrm{eq}} + x_{\mathrm{ML}}$ (Fig. 3, dashed line), in which case the next ML will form quasi-instantaneously. However, this probability may be extremely low, as will be discussed later.

Achieving quasideterministic growth despite the randomness of nucleation events and waiting times is important. Controlling the length of a NW section to within 1 ML is crucial in quantum axial heterostructures, be they based on alternating different materials (or alloys of different compositions [24]) or different crystal structures of the same material (crystal phase heterostructures [25–28]). Although the instant feedback offered by *in situ* TEM allows one to tailor at least the latter type of structures by changing the droplet contact angle [7], finding growth conditions minimizing intrinsic length fluctuations would open the way for producing them blindly in a standard growth setup devoid of real time *in situ* monitoring, simply by selecting the appropriate growth time, with which the section length would scale.

B. The mixed regime

We previously performed detailed measurements of the propagation and waiting times in a single NW at different growth temperatures, using the NanoMAX *in situ* TEM facility [8]. The observation of fractional MLs after each nucleation was compatible with an IML regime. At the lowest growth temperature, we found some evidence of self-regulation: the τ_c-distribution was narrower than expected for independent waiting and propagation times (as also observed in the vapor-solid-solid growth of II-VI NWs [9]), although not the very narrow distribution anticipated from the above considerations. This is in large part due to the limited time resolution of our experiments and we discussed other possible experimental and intrinsic sources of fluctuations. In addition to numerical growth simulations, we performed analytical calculations of the distributions of the various characteristic times [w, p and the ML cycle time, which can be measured between ML completions (τ_c) or between nucleations (τ_n; see Fig. 1), with possibly very different statistics [8]], albeit only in the strict IML regime and at low temperature, i.e., precisely under assumptions (A1) and (A2) above.

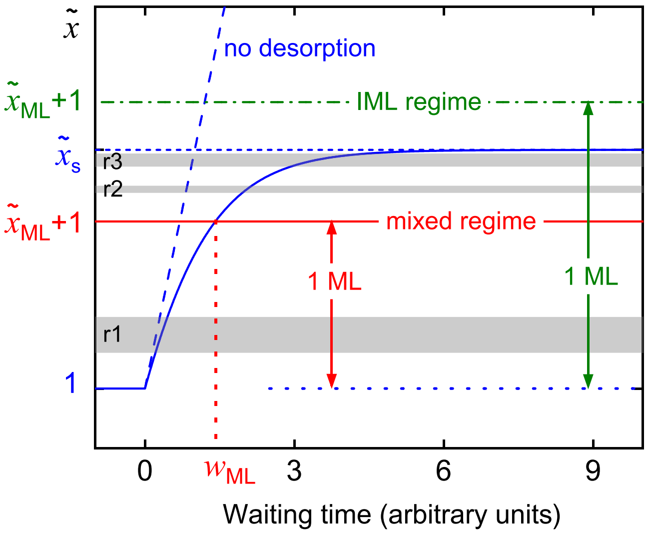

FIG. 3. Schematics of the variation of the reduced As concentration $\tilde{x}$ in the droplet with waiting time before nucleation. $\tilde{x}$ cannot exceed concentration $\tilde{x}_s$ at which desorption balances input. Concentration $\tilde{x}_{\mathrm{ML}} + 1$ corresponds to 1 ML worth of As available in the liquid. If $\tilde{x}_{\mathrm{ML}} + 1 > \tilde{x}_s$, the system is surely in the IML regime (green lines). If not, there is a finite probability that the waiting time exceeds w_{ML} (at which 1 ML becomes available in the liquid) and the mixed regime prevails (red lines), as is also the case in the absence of desorption. The figure remains valid if waiting time starts at $\tilde{x} > 1$. r1, r2, r3 are the nucleation ranges discussed in Sec. VII.

However, due to the stochasticity of nucleation, the waiting time and thus the initial droplet content is different for each ML, and we need not be in either of the extreme CML or IML regimes. We have just shown that the IML regime is necessary for strict self-regulation (identical τ_c for each ML), but it is important to evaluate quantitatively the deviation from this ideal situation depending on deviation from the IML regime.

The present work is devoted to this most general case of a *mixed regime*, with enough atoms in the liquid to form a complete ML at some nucleation events and not enough at others [labeled (c) and (i), respectively, in Fig. 1(b)]. We concentrate on analytical calculations, which allow us to explore wide ranges of parameters without any lengthy growth simulation. Such calculations are more difficult than for the strict IML regime (with systematic reset) studied previously [8] because of the correlations between successive MLs: after a type (c) event, the next cycle starts at a higher concentration than after a type (i) event, which will tend to shorten the waiting time [Fig. 1(b)]. We also lift further restrictions that limited the scope of our previous works. Namely, we allow for three possible nucleation loci on the NW hexagonal top facet. Most importantly, we include desorption from the liquid and thereby extend our analytical calculations of the statistical properties of the distributions of the various characteristic times to the whole temperature range.

III. MODEL

A. Monolayer cycle and desorption

As recalled above, each ML cycle can be decomposed into three stages [8,21]. Right after nucleation, the coverage θ of the interface by the new ML first increases abruptly (stage 1). This transfer of As atoms to the ML depletes the liquid and reduces its supersaturation. In the mixed regime [Fig. 1(b)], the two following situations occur:

(i) If there is not enough As in the liquid at nucleation to form a full ML, fast initial growth stage 1 ends when the liquid reaches equilibrium with the ML [21,29]. We assume that the As concentration at this point can be taken as the equilibrium concentration x_{eq} with the *bulk* solid. This is justified if the ML edge energy is low enough [21] and it simplifies the calculations, since x_{eq} depends only on temperature (and not on the shape and size of the fractional ML). Hence, in terms of the reduced As concentration $\tilde{x} = x/x_{\mathrm{eq}}$ (hereinafter "concentration"), $\tilde{x} = 1$ at the end of stage 1 [events (i) in Fig. 1(b)]. Assuming that nucleation took place at concentration $\tilde{x}_0$, case (i) thus occurs when $\tilde{x}_0 < \tilde{x}_{\mathrm{ML}} + 1$, with $\tilde{x}_{\mathrm{ML}} = x_{\mathrm{ML}}/x_{\mathrm{eq}}$. A low enough ML edge energy also allows us to assume that, during ML propagation (stage 2), x remains fixed to x_{eq} [21], which means that all As atoms fed to the droplet and not lost via desorption serve to extend the ML.

(c) Conversely, if $\tilde{x}_0 \geqslant \tilde{x}_{\mathrm{ML}} + 1$ at nucleation, there is enough As available in the liquid for a full ML to form at stage 1, at the end of which $\tilde{x} = \tilde{x}_0 - \tilde{x}_{\mathrm{ML}}$, stage 2 vanishes and $p = 0$ [events (c) in Fig. 1(b)].

In both cases, once the ML is complete, no further growth occurs over a finite waiting time w (stage 3), during which the droplet refills before the next nucleation. In experiments reported previously (where only case (i) was observed), we could not detect any ML propagation during stage 1 [5,8], which means that the time between nucleation and reaching equilibrium is surely very short with respect to characteristic times p and w. In the following, we simply assume that stage 1 is instantaneous, both in cases (i) (as previously [8]) and (c).

At stage 3, concentration $\tilde{x}$ first increases, which increases the desorption rate. However, $\tilde{x}$ cannot exceed the value $\tilde{x}_s$ at which desorption balances the external As input (Fig. 3). At variance with x_{eq}, $\tilde{x}_s$ is not an intrinsic quantity but depends on NW geometry and vapor flux in addition to temperature.

More precisely, the rate of desorption from the liquid of any molecule is proportional to its equilibrium pressure with this liquid [30], which increases with composition and temperature [17]. On the basis of available thermodynamic data [31], we find that, at least in the case of As, the equilibrium pressure of the group V dimers (As_2) is much larger than those of all other species (such as As or As_4) [17]. Desorption then occurs overwhelmingly via dimers, and since their equilibrium pressure very nearly scales with the square of the liquid composition (see below), so does the desorption rate [21]. During waiting time, $\tilde{x}$ thus obeys equation

$$\frac{d\tilde{x}}{dt} = V - D\tilde{x},^2 \tag{1}$$

with V the constant input rate of As into the liquid in terms of $\tilde{x}$ and D a desorption coefficient (to be calculated below). Then, if concentration is $\tilde{x}_1$ at time $t = 0$, in the absence of nucleation, concentration $\tilde{x}$ at a later time t is such that $t = \widehat{t}(\tilde{x}_1, \tilde{x})$ with

$$\widehat{t}(\tilde{x}_1, \tilde{x}) = \frac{1}{2\alpha V}\left[\ln\frac{1+\alpha u}{1-\alpha u}\right]_{u=\tilde{x}_1}^{u=\tilde{x}} \tag{2}$$

and $\alpha = (D/V)^{1/2}$. Concentration thus varies with time as

$$\widehat{\tilde{x}}(\tilde{x}_1, t) = \frac{1}{\alpha}\frac{F(\tilde{x}_1)e^{2\alpha V t} - 1}{F(\tilde{x}_1)e^{2\alpha V t} + 1}. \tag{3}$$

with

$$F(u) = \frac{1+\alpha u}{1-\alpha u}, \tag{4}$$

and it remains less than $\tilde{x}_s = 1/\alpha = (V/D)^{1/2}$.

$\widehat{t}$ and $\widehat{\tilde{x}}$ are inverse functions that describe the evolution of the composition starting from a given value $\tilde{x}_1$. This evolution (but not $\tilde{x}_1$) is independent of the previous history of the system and remains deterministic until the next nucleation.

Coefficients V and D can be expressed using the system parameters. Assuming a Knudsen evaporation coefficient equal to one (i.e., that all molecules impinging the liquid surface escape to the vapor) [17,30], the atomic desorption flux writes

$$J_e = \frac{2p_2}{\sqrt{2\pi M k_B T}}, \tag{5}$$

with M the mass of the As dimers and $p_2(T, x)$ their equilibrium pressure with a (Ga,As) liquid of composition x [17]. Calculations using the thermodynamic data of Ansara *et al.* [31] for bulk phases confirm that, at a given temperature, the quadratic approximation $p_2 = A_d(T)x^2$ leading to Eq. (1) is very good [17].

We consider a NW with hexagonal section of radius (side) R and a spherical cap droplet with base radius R_b and contact angle β (Fig. 2), which determine its radius R_d, outer area S_d and volume V_d [17]. This geometry allows us to consider various nucleation loci on the NW top facet [see Figs. 2(b)–2(d) and Sec. III B] while retaining the possibility of analytical calculations. We mitigate the resulting shape mismatch by writing $R_b = \alpha_b R$, with $\alpha_b \simeq 1$ a constant that can be chosen according to different possible rules. In all following calculations, we take $\alpha_b = 3^{3/4}/(2\pi)^{1/2} \simeq 0.90939$. This corresponds to equating the areas of NW top facet and base of the spherical cap [Fig. 2(b), dashed circle], which reduces the mismatch as compared with the simple choice $\alpha_b = 1$ [Fig. 2(b), dash-dotted circle]. The atomic desorption current is $J_e S_d$ and $N_{\mathrm{As}}^L = \tilde{x} x_{\mathrm{eq}} V_d/\Omega$, with $\Omega = V_d/N_{\mathrm{tot}}^L$ the average atomic volume in the liquid. Hence,

$$D = \frac{c_1(T)g_1(\beta)}{R}, \tag{6}$$

with $c_1(T) = 12A_d x_{\text{eq}}\,\Omega\alpha_b^{-1}/\sqrt{2\pi M k_B T}$ and $g_1(\beta) = \sin\beta/[(1-\cos\beta)(2+\cos\beta)]$.

On the other hand, $V = V_{\text{ML}}\tilde{x}_{\text{ML}}$, with V_{ML} the input rate in terms of MLs per unit time and

$$\tilde{x}_{\text{ML}} = \frac{c_2(T)g_2(\beta)}{R}, \tag{7}$$

with $c_2(T) = 6\Omega/[\alpha_b^3 a^2 x_{\text{eq}}]$ (where Ω, lattice parameter a and x_{eq} depend on temperature) and $g_2(\beta) = 3\sin^3\beta/[\pi(1-\cos\beta)^2(2+\cos\beta)]$.

From the GaAs thermodynamic data [31], we find the fits $\ln A_d(T) = -88.66682 + 0.22027T - 1.88842 \times 10^{-4}T^2 + 5.99272 \times 10^{-8}T^3$ and $\ln x_{\text{eq}}^{\text{ZB}}(T) = -41.59917 + 0.06611T - 2.94528 \times 10^{-5}T^2$ for the zinc blende (ZB) phase, for $500\text{ K} \leqslant T \leqslant 900\text{ K}$. Even better values can be obtained by fitting the same data at a given temperature over the restricted composition range effectively explored by the system (see Sec. VI B).

B. Nucleation rate and nucleation locus

In the framework of classical nucleation theory (CNT) adapted to nanostructures, we can take into account various possible nucleation loci by writing the probability of nucleation per unit time as [17,32]

$$P_n = J_n\Sigma_n, \tag{8}$$

with Σ_n the area available for nucleation (see below) and J_n the composition-dependent two-dimensional (2D) nucleation rate (per unit area and unit time) [17,33]:

$$J_n = Ax\left(\frac{\Delta\mu}{k_B T}\right)^{1/2}\exp\left(-\frac{\Delta G_c}{k_B T}\right). \tag{9}$$

In Eq. (9), prefactor A is independent of composition but may depend on temperature, $\Delta\mu$ is the difference of chemical potential per III-V pair between the liquid of composition x and binary solid, ΔG_c is the nucleation barrier and k_B is Boltzmann's constant. Recall that, in Eq. (9), the term $x[\Delta\mu/(k_B T)]^{1/2}$ originates from jointly accounting for the attachment rate to the critical nucleus and for the Zeldovich factor [33]. The 1 ML high nuclei have linear size r, perimeter $\alpha_1 r$ and area $\alpha_2 r^2$, with α_1, α_2 constants depending on the nucleus shape. The size of the critical nucleus is $r_c = b/\Delta\mu$ and the nucleation barrier is $\Delta G_c = B/\Delta\mu$, with $b = \alpha_1 a^3\gamma_e/(8\alpha_2)$ and $B = \alpha_1^2 a^4\gamma_e^2/(16\sqrt{3}\alpha_2)$. Here, γ_e the average effective surface energy of the vertical edge of the nucleus (see below) and a the ZB lattice parameter (assuming NWs growing along the $\langle 111\rangle$ ZB or $\langle 0001\rangle$ WZ axes and neglecting the differences of lattice spacings and pair volumes between ZB and WZ).

The 2D nucleus may form at different nonequivalent positions in the solid-liquid interface, corresponding to different areas Σ_n (Fig. 2). This is crucial for growth, and in particular for polytypism [13]. Nucleation can occur equiprobably over the whole interface, of area $S_H = 3\sqrt{3}R^2/2$ [Fig. 2(b)], and then $\Sigma_n = S_H$, or only in a narrow band along the triple phase line (TPL) boundary of the interface (of length $P_H = 6R$), the width of which scales with the critical radius [Fig. 2(c)] [13,32]. In both cases, we consider equilateral triangular nuclei of side r, which mimic the symmetry of the (111) plane [13]. In the second case, the width of the band is the altitude of the critical nucleus. Our previous work (based on molecular beam epitaxy experiments) shows that nucleation can even be restricted to the vicinity of the hexagon corners, with rhomboidal nuclei [Fig. 2(d)] [5] (a similar geometry was recently observed using chemical vapor epitaxy [34]). In this special case of nucleation at the TPL, and with equiprobable corners (as reported in Ref. [34]), Σ_n is simply six times the critical nucleus area $\sqrt{3}r_c^2/2$. The parameters α_1, α_2 defining the geometry of the nucleus and the expressions of Σ_n are listed in Table I, along with expressions for energy γ_e, including contributions from the step portions in contact with liquid (with energy γ_{nL} per unit area) and vapor. The latter is an effective value γ_{nV}^{eff} accounting for the liquid area eliminated when the nucleus forms at the TPL [8,13] (Fig. 2). Note that the nucleation rate [Eq. (9)] depends on nucleation shape and locus via ΔG_c.

TABLE I. Parameters relative to the three possible nucleation loci and associated nucleus shapes and effective edge energies. The triangle is equilateral and the rhomboid angles are $\pi/3$ and $2\pi/3$. r_c: side of critical nucleus; P_H, S_H: perimeter and area of the NW top facet. γ_{nL}, γ_{nV}^{eff}: energy per unit area of the nucleus-liquid and nucleus-vapor lateral interfaces.

Locus shape	Interface triangle	TPL triangle	Corner rhomboid
α_1	3	3	4
α_2	$\sqrt{3}/4$	$\sqrt{3}/4$	$\sqrt{3}/2$
Σ_n	S_H	$P_H r_c\sqrt{3}/2$	$6\alpha_2 r_c^2$
κ	$1/2$	$-1/2$	$-3/2$
η	0	1	2
χ	$3\sqrt{3}/2$	$3\sqrt{3}$	6
γ_e	γ_{nL}	$(2\gamma_{nL} + \gamma_{nV}^{\text{eff}})/3$	$(\gamma_{nL} + \gamma_{nV}^{\text{eff}})/2$

In addition, as discussed previously, for III-V compounds, at a given temperature T, $\Delta\mu$ is very well approximated by expression

$$\widehat{\Delta\mu}(x, T) = \alpha_\mu k_B T\ln(\tilde{x}), \tag{10}$$

with α_μ a temperature-dependent constant very close to one [8,17]. The equilibrium concentration, which appears in the definition of $\tilde{x}$, also depends on temperature (and on group III concentration in the liquid for metal-catalyzed growth [15]) and on crystal phase. Equation (10) implies that $x_{\text{eq}}^{\text{WZ}} = x_{\text{eq}}^{\text{ZB}}\exp[\delta E_{\text{coh}}/(\alpha_\mu k_B T)]$, with δE_{coh} the difference of cohesive energy between the two phases ($\delta E_{\text{coh}} = 24$ meV/pair for GaAs [35]). Given that the planar solid-liquid interface cooccurs with WZ in GaAs NWs [4,5,7,8], we take $x_{\text{eq}} = x_{\text{eq}}^{\text{WZ}}$ and, on the basis of previous work [5,34], assume corner nucleation [Fig. 2(d)].

From Eqs. (8)–(10), using the expressions of Σ_n for the three nucleation loci (Table I) and recalling that $r_c = b/\Delta\mu$ and $\Delta G_c = B/\Delta\mu$ (with b and B given above), we obtain the general expression

$$P_n(\tilde{x}) = A_c\tilde{x}(\ln\tilde{x})^\kappa\exp\left(-\frac{B_T}{\ln\tilde{x}}\right), \tag{11}$$

with

$$A_c = \chi A x_{\text{eq}}\, \alpha_\mu^\kappa b_T^\eta R^{2-\eta}, \tag{12}$$

$$b_T = (k_B T)^{-1} b, \tag{13}$$

$$B_T = \alpha_\mu^{-1}(k_B T)^{-2} B, \tag{14}$$

and parameters χ, κ, and η given in Table I for each nucleation locus. Note that the different dependencies on $\ln \tilde{x}$ result from the fact that the critical radius appears in Σ_n with exponents 0, 1, and 2 for the three nucleation loci, respectively.

The finite size of the top facet imposes a maximum critical nucleus size and hence a minimum value of $\Delta\mu$ at nucleation. This in turn sets a minimum value $\tilde{x}_{\min}$ of $\tilde{x}$ at nucleation, namely, $\exp[b_T/(\alpha_\mu R)]$ for corner or TPL nucleation and $\exp[b_T/(\sqrt{3}\alpha_\mu R)]$ for the full top facet, but these are only marginally larger than one.

During waiting time, concentration x varies significantly and subcritical clusters form and dissolve. We expect the lifetime of such clusters to be much shorter than w, which justifies considering the nucleation probability as a slowly varying function of instantaneous concentration in Eqs. (8)–(11).

IV. PROBABILITY DENSITY OF THE CONCENTRATION AT NUCLEATION

A. Definitions and governing equation

In a given NW, successive nucleation events occur at different values of the concentration $\tilde{x}$. We define the *probability density of the concentration at nucleation*, function $\pi_{\tilde{x}}$, such that, over the entire growth sequence of this NW (ideally infinite), the probability that nucleation occurs at concentration $\tilde{x}$, within interval $\delta\tilde{x}$, is $\pi_{\tilde{x}}(\tilde{x})\delta\tilde{x}$. We show in Sec. V that the statistical properties of all characteristic times, namely, p, w, τ_c, and τ_n, can be calculated from $\pi_{\tilde{x}}$. In the present section, we derive a differential equation governing this function.

To this end, we first define four related conditional probability densities. The first two, $\pi_w^{(1)}(w|\tilde{x}_1)$ for waiting time w and $\pi_{\tilde{x}}^{(1)}(\tilde{x}|\tilde{x}_1)$ for concentration $\tilde{x}$ at which nucleation occurs, are conditional to concentration being $\tilde{x}_1$ at the start of the waiting time. They are related by

$$\pi_w^{(1)}(w|\tilde{x}_1)dw = \pi_{\tilde{x}}^{(1)}(\tilde{x}|\tilde{x}_1)d\tilde{x}, \tag{15}$$

with $w = \widehat{t}(\tilde{x}_1, \tilde{x})$ or $\tilde{x} = \widehat{\tilde{x}}(\tilde{x}_1, w)$ and $d\tilde{x}/dw$ given by Eq. (1). Density $\pi_w^{(1)}$ is obtained from the nucleation probability [Eq. (11)] and the increase of concentration during waiting time [Eq. (3)] [8,20,36]:

$$\pi_w^{(1)}(w|\tilde{x}_1) = P_n(\widehat{\tilde{x}}(\tilde{x}_1, w)) \exp\left\{-\int_0^w P_n(\widehat{\tilde{x}}(\tilde{x}_1, t))dt\right\}. \tag{16}$$

The last two densities, $\pi_w^{(0)}(w|\tilde{x}_0)$ and $\pi_{\tilde{x}}^{(0)}(\tilde{x}|\tilde{x}_0)$, are conditional to the previous nucleation having occurred at concentration $\tilde{x}_0$. The pairs are thus linked by

$$\pi_u^{(0)}(u|\tilde{x}_0) = \pi_u^{(1)}[u, \tilde{x}_1(\tilde{x}_0)] \quad \text{for } u = \tilde{x} \text{ or } w, \tag{17}$$

with $\tilde{x}_1(\tilde{x}_0) = 1$ in case (i) and $\tilde{x}_1(\tilde{x}_0) = \tilde{x}_0 - \tilde{x}_{\text{ML}}$ in case (c) [Fig. 1(b)].

Using Eqs. (16), (15), and (17), we obtain

$$\pi_{\tilde{x}}^{(0)}(\tilde{x}|\tilde{x}_0) = Q_n(\tilde{x}) \exp\left[-\int_{\tilde{x}_1(\tilde{x}_0)}^{\tilde{x}} Q_n(u)du\right], \tag{18}$$

where

$$Q_n(\tilde{x}) = \frac{P_n(\tilde{x})}{V(1-\alpha^2\tilde{x}^2)}. \tag{19}$$

Equation (18) holds if $\tilde{x}_1(\tilde{x}_0) \leqslant \tilde{x} < \tilde{x}_s$; if not, $\pi_{\tilde{x}}^{(0)}(\tilde{x}|\tilde{x}_0) = 0$.

Function $\pi_{\tilde{x}}$ must satisfy the following integral equation:

$$\pi_{\tilde{x}}(\tilde{x}) = \int_{\tilde{x}_{\inf}(\tilde{x})}^{\tilde{x}_{\sup}(\tilde{x})} \pi_{\tilde{x}}^{(0)}(\tilde{x}|\tilde{x}_0)\pi_{\tilde{x}}(\tilde{x}_0)d\tilde{x}_0. \tag{20}$$

The integration limits are found by noting that a nucleation at $\tilde{x}$ can follow any nucleation at $\tilde{x}_0$ such that $\tilde{x}_1(\tilde{x}_0) \leqslant \tilde{x}$, i.e., $\tilde{x}_0 \leqslant \tilde{x}_{\text{ML}} + 1$ in case (i) and $1 \leqslant \tilde{x}_0 - \tilde{x}_{\text{ML}} \leqslant \tilde{x}$ in case (c). Hence, $\tilde{x}_{\inf}(\tilde{x}) = \tilde{x}_{\min} \simeq 1$, $\tilde{x}_{\sup}(\tilde{x}) = \min(\tilde{x} + \tilde{x}_{\text{ML}}, \tilde{x}_s) = m_1(\tilde{x})$. Equation (20) becomes

$$\pi_{\tilde{x}}(\tilde{x}) = \frac{Q_n(\tilde{x})}{H(\tilde{x})}\left[\pi_{\text{ML}} + \int_{\tilde{x}_{\text{ML}+1}}^{m_1(\tilde{x})} H(\tilde{x}_0 - \tilde{x}_{\text{ML}})\pi_{\tilde{x}}(\tilde{x}_0)d\tilde{x}_0\right], \tag{21}$$

with

$$H(\tilde{x}) = \exp\left(\int_{\tilde{x}_{\min}}^{\tilde{x}} Q_n(u)du\right), \tag{22}$$

$$\pi_{\text{ML}} = \int_{\tilde{x}_{\min}}^{\tilde{x}_{\text{ML}}+1} \pi_{\tilde{x}}(\tilde{x}_0)d\tilde{x}_0. \tag{23}$$

π_{ML} is thus the fraction of type (i) nucleation events. In the IML regime, where $\tilde{x}_s < \tilde{x}_{\text{ML}} + 1$, the upper integration limit in Eq. (23) is $\tilde{x}_s$ and the integral in Eq. (21) cancels. We now consider the proper mixed regime.

Since function $\pi_{\tilde{x}}$ may diverge when $\tilde{x} \to \tilde{x}_s$, we prefer handling function K, defined by

$$K(\tilde{x}) = V(1-\alpha^2\tilde{x}^2)\pi_{\tilde{x}}(\tilde{x}), \tag{24}$$

in terms of which Eq. (21) becomes

$$K(\tilde{x}) = \phi(\tilde{x})\left[\pi_{\text{ML}} + \int_{\tilde{x}_{\text{ML}}+1}^{m_1(\tilde{x})} \frac{H(\tilde{x}_0 - \tilde{x}_{\text{ML}})}{V\left(1-\alpha^2\tilde{x}_0^2\right)}K(\tilde{x}_0)d\tilde{x}_0\right], \tag{25}$$

with

$$\phi(\tilde{x}) = [H(\tilde{x})]^{-1}P_n(\tilde{x}). \tag{26}$$

Integral equation (25) is finally rewritten as a differential equation:

$$\begin{aligned}\frac{dK}{d\tilde{x}} &= \frac{d\ln\phi(\tilde{x})}{d\tilde{x}}K(\tilde{x})\\ &\quad + \frac{\phi(\tilde{x})H(m_1(\tilde{x}) - \tilde{x}_{\text{ML}})}{V[1-\alpha^2(\tilde{x}+\tilde{x}_{\text{ML}})^2]}\frac{dm_1}{d\tilde{x}}K(m_1(\tilde{x})).\end{aligned} \tag{27}$$

B. Semi-analytical solution

Solving Eq. (27) requires in particular calculating function H, from which function ϕ [Eq. (26)] and its derivative can be obtained. To this end, we derive analytical expressions for the three different nucleation loci. From Eq. (22) and a series expansion of the denominator of Q_n [Eq. (19)], we find, by using the general expression (11) of the nucleation probability, that

$$\ln H(\tilde{x}) = A_c \sum_{q=0}^{\infty} \alpha^{2q} L_q(\tilde{x}), \tag{28}$$

with

$$L_q(\tilde{x}) = \int_{\tilde{x}_{\min}}^{\tilde{x}} u^{2q+1} (\ln u)^{\kappa} \exp\left(-\frac{B_T}{\ln u}\right) du. \tag{29}$$

We consider in turn the three nucleation loci.

1. Corner nucleation ($\kappa = -3/2$, superscript c)

Setting $f(\tilde{x}) = (\ln \tilde{x})^{-1/2}$, we get

$$L_q^c(\tilde{x}) = 2 \int_{f(\tilde{x})}^{f(\tilde{x}_{\min})} \exp\left(\frac{2(q+1)}{v^2} - B_T v^2\right) dv, \tag{30}$$

and, using result 7.4.34 in Ref. [37],

$$L_q^c(\tilde{x}) = \sqrt{\frac{\pi}{4B_T}} \left\{ e^{\frac{2(q+1)}{v^2} - B_T v^2} \left[\omega\left(\frac{\sqrt{2(q+1)}}{v} + i\sqrt{B_T}\, v\right) + \omega\left(-\frac{\sqrt{2(q+1)}}{v} + i\sqrt{B_T}\, v\right) \right] \right\}_{f(\tilde{x}_{\min})}^{f(\tilde{x})}, \tag{31}$$

with i the imaginary unit and ω the Faddeeva-Kramp function [37–39], already encountered in our calculation for corner nucleation with no desorption [8]. Given the symmetries of function ω [37], this can be rewritten as

$$L_q^c(\tilde{x}) = \sqrt{\frac{\pi}{B_T}} [\mathrm{Re}\{\psi_q[f(\tilde{x})]\} - \mathrm{Re}\{\psi_q[f(\tilde{x}_{\min})]\}], \tag{32}$$

where Re denotes the real part of a complex number and

$$\psi_q(v) = e^{\frac{2(q+1)}{v^2} - B_T v^2} \omega\left(\frac{\sqrt{2(q+1)}}{v} + i\sqrt{B_T}\, v\right). \tag{33}$$

Recall that $\tilde{x}_{\min}$ is close to one, a value for which $f(\tilde{x}) \to \infty$ and $\psi_q[f(\tilde{x})]$ cancels. For $q = 0$, Eqs. (32) and (33) coincide with our previous calculation in absence of desorption [8].

2. TPL nucleation ($\kappa = -1/2$, superscript TPL)

Here, with change of variable $v = f^{-1}(u)$,

$$L_q^{\mathrm{TPL}}(\tilde{x}) = 2 \int_{f^{-1}(\tilde{x}_{\min})}^{f^{-1}(\tilde{x})} \exp\left(2(q+1)v^2 - \frac{B_T}{v^2}\right) dv, \tag{34}$$

and, using result 7.4.33 in Ref. [37],

$$L_q^{\mathrm{TPL}}(\tilde{x}) = \sqrt{\frac{\pi}{2(q+1)}} (\mathrm{Im}\{\psi_q[f(\tilde{x})]\} - \mathrm{Im}\{\psi_q[f(\tilde{x}_{\min})]\}), \tag{35}$$

where Im denotes the imaginary part of a complex number and $\mathrm{Im}\{\psi_q[f(\tilde{x}_{\min})]\} \simeq 0$.

3. Nucleation over the whole top facet ($\kappa = 1/2$, superscript HEX)

In this case, a simple integration by parts yields

$$L_q^{\mathrm{HEX}}(\tilde{x}) = \frac{1}{2(q+1)} \left[h_q(\tilde{x}) - B_T L_q^c(\tilde{x}) - \frac{1}{2} L_q^{\mathrm{TPL}}(\tilde{x}) \right], \tag{36}$$

with

$$h_q(\tilde{x}) = \tilde{x}^{2(q+1)} (\ln \tilde{x})^{1/2} \exp\left(-\frac{B_T}{\ln \tilde{x}}\right). \tag{37}$$

Here, $h_q(\tilde{x}_{\min}) = 0$ if $\tilde{x}_{\min}$ is set to one.

The alternative analytical expressions (32), (35), and (36), each pertaining to a particular nucleation locus, can be evaluated using efficient numerical implementations of the Faddeeva function [39], and then summed in series [Eq. (28), where we use up to 500 000 terms] to yield values of functions H and ϕ at any point. These values are used in the numerical solution of differential equation (27), which proceeds as follows.

From Eq. (24), $K(\tilde{x}) = 0$ for $\tilde{x} \geqslant \tilde{x}_s$. For $\tilde{x}_{\min} \leqslant \tilde{x} < \tilde{x}_s$, the equation can be solved sequentially in at most two main descending intervals.

If $\tilde{x}_s - \tilde{x}_{\mathrm{ML}} \leqslant \tilde{x} < \tilde{x}_s$, $m_1(\tilde{x}) = \tilde{x}_s$, $dm_1/d\tilde{x} = 0$ and Eq. (27) reduces to $d \ln K/d\tilde{x} = d \ln \phi/d\tilde{x}$. Thus, $K(\tilde{x}) = C\phi(\tilde{x})$, with C an integration constant to be determined. Of course, resolution is completed if $\tilde{x}_s - \tilde{x}_{\mathrm{ML}} \leqslant \tilde{x}_{\min}$.

If not, Eq. (27) is solved numerically in the remaining interval $[\tilde{x}_{\min}, \tilde{x}_s - \tilde{x}_{\mathrm{ML}}]$. There, $m_1(\tilde{x}) = \tilde{x} + \tilde{x}_{\mathrm{ML}}$ and Eq. (27) is akin to a delay differential equation, since the derivative at the current point depends on the function value at a point translated by a fixed quantity, namely, $\tilde{x}_{\mathrm{ML}}$. The solution is thus computed in descending subintervals of width $\tilde{x}_{\mathrm{ML}}$. In each subinterval, the solution is calculated at any desired discrete set of points by an IMSL routine [40], which requires to have available the coefficients of the differential equation at any point in the subinterval. In the uppermost subinterval $[\tilde{x}_s - 2\tilde{x}_{\mathrm{ML}}, \tilde{x}_s - \tilde{x}_{\mathrm{ML}}]$, these are readily obtained from the calculation of H and by noting that $K(\tilde{x} + \tilde{x}_{\mathrm{ML}}) = C\phi(\tilde{x} + \tilde{x}_{\mathrm{ML}})$. In the subinterval below, $[\tilde{x}_s - 3\tilde{x}_{\mathrm{ML}}, \tilde{x}_s - 2\tilde{x}_{\mathrm{ML}}]$ (if needed), $K(\tilde{x} + \tilde{x}_{\mathrm{ML}})$ is obtained for any $\tilde{x}$ by interpolation between the discrete points of subinterval $[\tilde{x}_s - 2\tilde{x}_{\mathrm{ML}}, \tilde{x}_s - \tilde{x}_{\mathrm{ML}}]$ where it has just been calculated. This process is repeated until the whole interval $[\tilde{x}_{\min}, \tilde{x}_s - 2\tilde{x}_{\mathrm{ML}}]$ has been treated. The whole solution is obtained modulo multiplicative constant C, which we finally determine by equating the integral of $\pi_{\tilde{x}}$ over $[\tilde{x}_{\min}, \tilde{x}_s]$ to one.

These calculations will be illustrated in Secs. VI B and VII. Once density $\pi_{\tilde{x}}$ is determined, the distributions of the various characteristic times can be calculated, as shown in the next section.

V. STATISTICS OF THE CHARACTERISTIC TIMES

A. Propagation time

All propagation times following a type (c) nucleation are zero. The fraction of these is $1 - \pi_{\mathrm{ML}}$. After a type (i) nucleation at droplet content $\tilde{x}_0 \leqslant \tilde{x}_{\mathrm{ML}} + 1$, an ML fraction corresponding to $\tilde{x}_0 - 1$ is quickly grown. During the following propagation time $p(\tilde{x}_0)$, the liquid remains at equilibrium with solid ($\tilde{x}=1$) and, from Eq. (1), the concentration $\tilde{x}$ available for extending the ML from the external source verifies $d\tilde{x}/dt = V_e$ with $V_e = (1-\alpha^2)V$ the net input rate (input minus desorption) at equilibrium. Hence,

$$p(\tilde{x}_0) = \frac{\tilde{x}_{\rm ML} - \tilde{x}_0 + 1}{V_e}. \tag{38}$$

The probability density of the propagation time, π_p, is such that $\pi_p(p)dp = -\pi_{\tilde{x}} d\tilde{x}_0$. Hence,

$$\pi_p(p) = V_e \pi_{\tilde{x}}(\tilde{x}_{\rm ML} + 1 - V_e p) \tag{39}$$

for $p \leqslant p_s$, with $p_s = p(\tilde{x}_{\min})$ (the largest possible propagation time), and $\pi_p(p) = 0$ for $p > p_s$.

B. Waiting time

The probability density of the waiting time is

$$\pi_w(w) = \int_{\tilde{x}_{\min}}^{\tilde{x}_s} \pi_w^{(0)}(w|\tilde{x}_0)\pi_{\tilde{x}}(\tilde{x}_0)d\tilde{x}_0. \tag{40}$$

We first express density $\pi_w^{(1)}$ in terms of functions H [Eqs. (22) and (28)] and ϕ [Eq. (26)], after change of variable $t \to \tilde{x} = \widehat{\tilde{x}}(\tilde{x}_1, t)$ [Eq. (3)] in the integral of Eq. (16):

$$\pi_w^{(1)}(w|\tilde{x}_1) = \phi(\widehat{\tilde{x}}(\tilde{x}_1, w))H(\tilde{x}_1). \tag{41}$$

$\pi_w^{(0)}(w|\tilde{x}_0)$ is then calculated from Eq. (17) and inserted into Eq. (40). Distinguishing again nucleation events at $\tilde{x}_0$ of types (i) $[\tilde{x}_1(\tilde{x}_0) = 1]$ and (c) $[\tilde{x}_1(\tilde{x}_0) = \tilde{x}_0 - x_{\rm ML}]$, we find that $\pi_w(w) = J_i(w) + J_c(w)$, where

$$J_i(w) = \pi_{\rm ML}\phi(\widehat{\tilde{x}}(1, w)), \tag{42}$$

$$J_c(w) = \int_{\tilde{x}_{\rm ML}+1}^{\tilde{x}_s} \pi_{\tilde{x}}(\tilde{x}_0)\phi(\widehat{\tilde{x}}(\tilde{x}_0 - \tilde{x}_{\rm ML}, w))H(\tilde{x}_0 - \tilde{x}_{\rm ML})d\tilde{x}_0. \tag{43}$$

Of course, $J_c = 0$ if $\tilde{x}_s \leqslant \tilde{x}_{\rm ML} + 1$ (IML regime).

C. Monolayer cycle time

Here, we exclude the strict IML regime (Sec. II A), which ensures that $\alpha(\tilde{x}_{\rm ML} + 1) < 1$. Consider a ML cycle starting with the completion of the preceding ML at $\tilde{x} = \tilde{x}_1$ and ending with ML completion after time τ_c. The ML nucleates within the cycle at concentration $\tilde{x} \geqslant \tilde{x}_1$, after waiting time $w = \widehat{t}(\tilde{x}_1, \tilde{x})$ [Eq. (2)]. If $\tilde{x} < \tilde{x}_{\rm ML} + 1$ [case (i)], the ML cycle comprises a nonzero propagation time and $\tau_c = \varphi(\tilde{x}_1, \tilde{x})$, with $\varphi(\tilde{x}_1, \tilde{x}) = \widehat{t}(\tilde{x}_1, \tilde{x}) + p(\tilde{x})$. If $\tilde{x} \geqslant \tilde{x}_{\rm ML} + 1$ [case (c)], then $p = 0$ and $\tau_c = \widehat{t}(\tilde{x}_1, \tilde{x})$.

Setting $\tau_m = \tilde{x}_{\rm ML}/V_e$ and $\tau_M = \widehat{t}(1, \tilde{x}_{\rm ML} + 1)$, we find (see Fig. 4) that case (i) requires $\tau_c \leqslant \tau_M$ and $\tilde{x}_1^-(\tau_c) \leqslant \tilde{x}_1 \leqslant \tilde{x}_1^+(\tau_c)$ with

$$\tilde{x}_1^-(\tau_c) = \begin{cases} \tilde{x}_{\rm ML} + 1 - V_e\tau_c, & \text{if } 0 \leqslant \tau_c \leqslant \tau_m \\ 1, & \text{if } \tau_m \leqslant \tau_c \leqslant \tau_M, \end{cases} \tag{44}$$

$$\tilde{x}_1^+(\tau_c) = \frac{1}{\alpha}\frac{F(\tilde{x}_{\rm ML} + 1)e^{-2\alpha V\tau_c} - 1}{F(\tilde{x}_{\rm ML} + 1)e^{-2\alpha V\tau_c} + 1} \quad \text{if } 0 \leqslant \tau_c \leqslant \tau_M, \tag{45}$$

with function F given by Eq. (4). Since

$$\frac{\partial\varphi}{\partial\tilde{x}} = \frac{\alpha^2(\tilde{x}^2 - 1)}{V_e(1 - \alpha^2\tilde{x}^2)}, \tag{46}$$

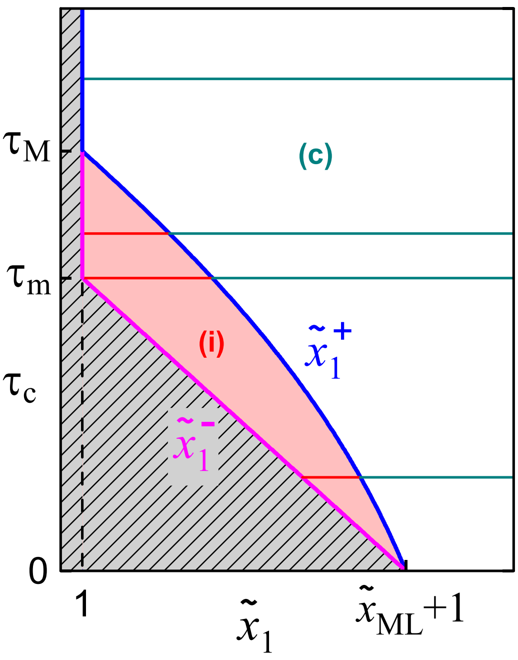

FIG. 4. Relationship between duration τ_c of ML cycle and droplet composition $\tilde{x}_1$ at its beginning. Couples $(\tilde{x}_1, \tau_c)$ in domains (i) (between curves $\tilde{x}_1^-$ and $\tilde{x}_1^+$, pink shaded) and (c) (above curve $\tilde{x}_1^+$) give rise to incomplete and complete MLs at nucleation within the cycle, respectively. The left borders of the domains ($\tilde{x}_1 = 1$) correspond to all nucleations having produced an incomplete ML during the previous ML cycle, and the inner parts to those having produced a complete ML, at concentration $\tilde{x}_1 + \tilde{x}_{\rm ML}$. The horizontal segments illustrate the allowed ranges of $\tilde{x}_1$ for a few values of τ_c. The striped shaded area is forbidden.

φ is a monotonically increasing function. Hence, for any $\tilde{x}_1$ within range $[\tilde{x}_1^-(\tau_c), \tilde{x}_1^+(\tau_c)]$, there is a single nucleation concentration $\tilde{x} = \tilde{x}^{(n)}(\tau_c, \tilde{x}_1)$ such that $\tau_c = \varphi(\tilde{x}_1, \tilde{x})$ (which can be expressed using the r-Lambert function [41]). Moreover, the probability density of the ML cycle time conditional to its start at concentration $\tilde{x}_1$, $\pi_{\tau_c}(\tau_c|\tilde{x}_1)$, verifies the equation

$$\pi_{\tau_c}(\tau_c|\tilde{x}_1)\frac{\partial\varphi}{\partial\tilde{x}}(\tilde{x}_1, \tilde{x}) = \pi_{\tilde{x}}^{(1)}(\tilde{x}|\tilde{x}_1). \tag{47}$$

Using Eqs. (15) and (41) and recalling that $\widehat{\tilde{x}}(\tilde{x}_1, \widehat{t}(\tilde{x}_1, \tilde{x})) = \tilde{x}$ and $\alpha = 1/\tilde{x}_s$, we replace $\pi_{\tilde{x}}(\tilde{x}|\tilde{x}_1)$ by $\phi(\tilde{x})H(\tilde{x}_1)\partial\widehat{t}/\partial\tilde{x}$ in this equation, which yields

$$\pi_{\tau_c}(\tau_c|\tilde{x}_1) = \frac{(\tilde{x}_s^2 - 1)H(\tilde{x}_1)}{[\tilde{x}^{(n)}(\tau_c, \tilde{x}_1)]^2 - 1}\phi(\tilde{x}^{(n)}(\tau_c, \tilde{x}_1)). \tag{48}$$

Case (c) occurs either when $\tau_c \leqslant \tau_M$ and $\tilde{x}_1 > \tilde{x}_1^+(\tau_c)$, or when $\tau_c > \tau_M$ for any $\tilde{x}_1$ (Fig. 4). The concentration at nucleation is then simply $\tilde{x} = \widehat{\tilde{x}}(\tilde{x}_1, \tau_c)$ and

$$\pi_{\tau_c}(\tau_c|\tilde{x}_1) = \frac{(\tilde{x}_s^2 - 1)(1 - \alpha^2\tilde{x}^2)H(\tilde{x}_1)}{\tilde{x}^2 - 1}\phi(\tilde{x}). \tag{49}$$

Finally, when $\tau_c < \tau_m$, values $\tilde{x}_1 < \tilde{x}_1^-(\tau_c)$ are excluded (part of striped shaded area in Fig. 4).

It now remains to take into account all possible values of $\tilde{x}_1$ at beginning of ML cycle (at given τ_c). Value $\tilde{x}_1 = 1$ has total probability $\pi_{\rm ML}$, corresponding to all previous nucleations at

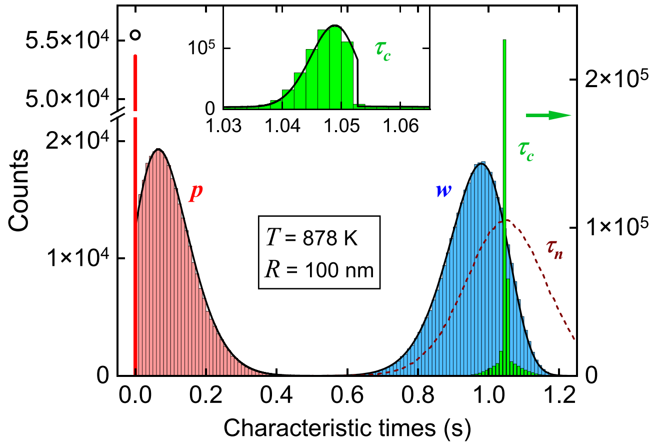

FIG. 5. Distributions of characteristic times for a self-catalyzed GaAs NW of radius $R = 100$ nm growing at $T = 878$ K under an input of 1 ML s^{-1} (with $\beta = 100^\circ$). The histograms of the waiting (w) and propagation (p) times and cycle times between ML completions (τ_c) are obtained by growth simulation (for a total of 381 654 MLs) and the corresponding curves (p, w) by semi-analytical calculation. The bar (simulation) and circle (calculation) at $p = 0$ give the number of complete MLs formed at nucleation, and the dashed curve the distribution of the ML cycle time between nucleations (τ_n). The inset shows in more detail the distributions of τ_c simulated (over twice the time) and calculated (curve).

$\tilde{x}_0$ of type (i), whereas values $\tilde{x}_1 > 1$ have probability density $\pi_{\tilde{x}}(\tilde{x}_1 + \tilde{x}_{\rm ML})$, corresponding to previous nucleations of type (c) (Fig. 4). Finally,

$$\pi_{\tau_c}(\tau_c) = \pi_{\rm ML}\pi_{\tau_c}(\tau_c|1) + \int_{\tilde{x}_1^-(\tau_c)}^{+\infty} \pi_{\tau_c}(\tau_c|\tilde{x}_1)\pi_{\tilde{x}}(\tilde{x}_1 + \tilde{x}_{\rm ML})d\tilde{x}_1. \tag{50}$$

Here, in the first term of the sum (which appears only if $\tau_c \geqslant \tau_m$), $\pi_{\tau_c}(\tau_c|1)$ is given by Eqs. (48) and (49) for $\tau_m \leqslant \tau_c \leqslant \tau_M$ and $\tau_c \geqslant \tau_M$, respectively; in the integral, $\pi_{\tau_c}(\tau_c|\tilde{x}_1)$ is given by Eqs. (48) and (49) for $\tilde{x}_1^-(\tau_c) \leqslant \tilde{x}_1 \leqslant \tilde{x}_1^+(\tau_c)$ and $\tilde{x}_1 \geqslant \tilde{x}_1^+(\tau_c)$, respectively (only the second case occurs for $\tau_c \geqslant \tau_M$).

For sake of completeness, we can also calculate the distribution of the ML cycle time τ_n between nucleation events. We find

$$\pi_{\tau_n}(\tau_n) = H(1)\int_0^{\tau_n} \pi_p(p)\phi(\widehat{\tilde{x}}(1, \tau_n - p))dp + J_c(w), \tag{51}$$

where the two terms of the sum correspond to initial nucleations of types (i) and (c), respectively.

Figure 5 illustrates the calculations of the various characteristic times, to be discussed further in Secs. VI B and VII, and the excellent agreement between simulations and semi-analytical results. Here and in all following calculations, we take $\beta = 100^\circ$ and use nucleation rate parameters (see Sec. III B) from our joint experimental and theoretical study of statistics of the characteristic times, namely, $\gamma_e = 0.206$ J m^{-2} and $\ln A(T) = \ln A(T_0) + E_a(T - T_0)/(k_B T_0 T)$, with $T_0 = 838$ K, $\ln A(T_0) = 59.5$, $E_a = 3.84$ eV, and A in m^{-2} s^{-1} [8].

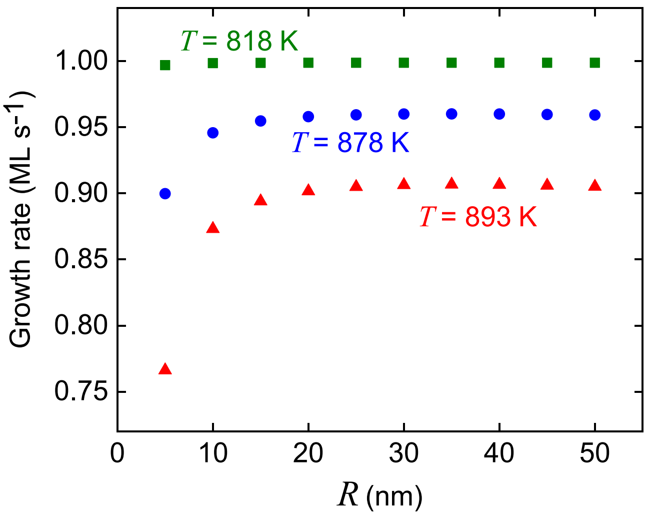

FIG. 6. Average growth rate of a self-catalyzed GaAs NW at different temperatures, as a function of NW radius, for an input $V_{\rm ML} = 1$ ML s^{-1} ($\beta = 100^\circ$).

During each ML cycle, the liquid explores a wide and variable concentration range and the desorption rate varies accordingly. Thus, the average growth rate cannot be calculated directly from input rate and temperature, as if concentration remained constant [17]. Instead, we find it as the inverse of the average ML cycle time $\langle\tau_c\rangle = \int_0^\infty \tau_c \pi_{\tau_c}(\tau_c)d\tau_c$. As an example, Fig. 6 shows, for a fixed input of 1 ML s^{-1}, the effect on $\langle\tau_c\rangle$ of the overall increase of desorption with temperature, which depends little on NW radius, apart from a strong enhancement in very thin NWs, due to the Kelvin effect.

VI. CRITERIA FOR THE INCOMPLETE MONOLAYER REGIME

A. Strict condition

As already noticed, without even calculating $\pi_{\tilde{x}}$, on the sole basis of Eqs. (1)–(4), we can be sure that the IML regime is realized if $\tilde{x}_s < \tilde{x}_{\rm ML} + 1$ (Fig. 3). We formulate this condition in terms of system geometry and growth conditions. Using the expressions of V and D [Eq. (6)] from Sec. III A, we find

$$\tilde{x}_s = c_3(T)\cos(\beta/2)V_{\rm ML}^{1/2}, \tag{52}$$

with

$$c_3(T) = \frac{1}{\alpha_b a x_{\rm eq}}\left(\frac{3\sqrt{2\pi M k_B T}}{\pi A_d}\right)^{1/2}. \tag{53}$$

Apparently, $\tilde{x}_s$ does not depend on R. Actually, $\tilde{x}_s$ results from a balance between input and desorption currents. In terms of numbers of atoms, the latter and the direct and re-emitted contributions to the former all scale with R^2. If these are the only input pathways, then $V_{\rm ML}$, and hence $\tilde{x}_s$, are truly R-independent, since $N_{\rm ML}$ also scales with R^2. If however diffusion (which scales with R) contributes to group V input [42], then $V_{\rm ML}$ depends on R. $V_{\rm ML}$ also depends on contact angle β, since input and desorption currents depend differently on it [42–44].

Equations (7) and (52) yield the condition for the IML regime as

$$c_3(T)\cos(\beta/2)V_{\rm ML}^{1/2} < 1 + \frac{c_2(T)g_2(\beta)}{R}. \tag{54}$$

This corresponds to low growth rates (for desorption to balance input at low enough concentration) and narrow NWs (a ML may then amount to a large fraction of the total As content of the droplet).

These calculations ignore the Kelvin and Gibbs-Thomson effects related to the curvature and small size of the droplet [17]. The Kelvin effect enhances desorption, since the equilibrium pressure of group V dimers over a liquid of any composition is multiplied by $\exp\widetilde{\Delta\mu}_K$, where $\widetilde{\Delta\mu}_K = 4\Omega_V\gamma_L\sin\beta/(R_b k_B T)$, with $\Omega_V \simeq \Omega$ the volume of a group V atom in the liquid and γ_L the surface tension of the liquid [17]. The VLS-specific Gibbs-Thomson effect results in the addition to $\Delta\mu$ of $\Delta\mu_{GT} = 2\delta\Omega_p\gamma_L\sin\beta/R_b$, with $\delta\Omega_p$ the difference of the volumes of a III-V pair between liquid and solid phases, which can be of either sign [17,32]. We can still write $\Delta\mu = \alpha_\mu k_B T\ln(\tilde{x})$ using modified concentration $\tilde{x} = x/x_{\rm eq}(R)$, where $x_{\rm eq}(R) = x_{\rm eq}\exp(-\widetilde{\Delta\mu}_{GT})$, with $x_{\rm eq}$ the bulk value and $\widetilde{\Delta\mu}_{GT} = \Delta\mu_{GT}/(\alpha_\mu k_B T)$. By considering desorption and input, we find that Eq. (1) still holds, provided we use this new variable and coefficients V and D are changed to $V(R) = Ve^{\widetilde{\Delta\mu}_{GT}}$ and $D(R) = De^{\widetilde{\Delta\mu}_K - \widetilde{\Delta\mu}_{GT}}$, respectively. Consequently, upper bound $\tilde{x}_s$ becomes $\tilde{x}_s(R) = \tilde{x}_s e^{\widetilde{\Delta\mu}_{GT} - \widetilde{\Delta\mu}_K/2}$. The condition for the IML regime is $\tilde{x}_s(R) < \tilde{x}_{\rm ML}(R) + 1$, with $\tilde{x}_{\rm ML}(R) = \tilde{x}_{\rm ML}e^{\widetilde{\Delta\mu}_{GT}}$. Small size effects thus complicate the simple inverse R-dependence of Eq. (54). Since the Gibbs-Thomson effect involves only a difference of atomic volumes, it has much less impact than the Kelvin effect. The modification tends to be modest for $x_{\rm eq}$, whereas desorption may increase and x_s decrease significantly (since $\Delta\mu_K > 0$). This greatly extends the IML regime domain, as shown in Fig. 7.

B. Statistical approach: The effective incomplete monolayer regime

Criterion (54) (modified for small size effects) may be unduly demanding. In practice, the incomplete ML regime only requires that $\pi_{\tilde{x}} \simeq 0$ for $\tilde{x} \geqslant \tilde{x}_{\rm ML} + 1$. We expect $\pi_{\tilde{x}}$ to be a function with a single maximum tending to zero at low and high values of $\tilde{x}$: for $\tilde{x}$ small (of course larger than one), $\Delta\mu$ is too low for nucleation to occur, whereas the high values cannot be reached since, due to the rapid increase of the nucleation rate with concentration, all nucleations occur at lower values.

This is illustrated in Fig. 8, where distribution $\pi_{\tilde{x}}$ is shown at two different growth temperatures and for widely different input rates in the droplet. In both cases, although $\tilde{x}_{\rm ML} + 1 < x_s$, which should in principle lead to the mixed regime, the IML regime effectively prevails, since $\pi_{\tilde{x}}$ becomes negligible for values of $\tilde{x}$ well below $\tilde{x}_{\rm ML} + 1$. Then, nearly all nucleation events give rise to an incomplete ML. It thus becomes interesting to investigate how NW geometry and growth conditions govern this effective IML regime. We propose two approaches.

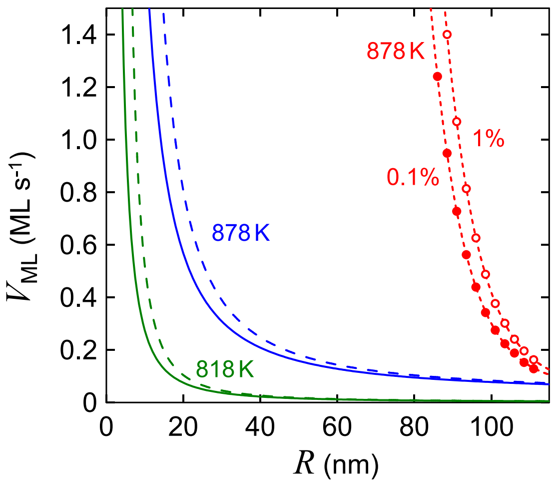

FIG. 7. Variation with NW radius of the input rate of As atoms in the droplet below which the strict condition for IML regime is realized, at growth temperatures of 818 K (green) and 878 K (blue). Full and dashed curves are obtained from semi-analytical calculations without and with small size effects, respectively. The proper IML domains lie under the curves. Symbols and red fitting curves correspond to effective IML regimes at $T = 878$ K: for $(R, V_{\rm ML})$ couples under the curves, less than 0.1% (disks) or 1% (circles) of the nucleation events produce a complete ML.

The As content of the droplet at nucleation may equivalently be defined in terms of concentration $\tilde{x}$ or of available fraction of ML, namely,

$$\theta = \frac{(\tilde{x}-1)x_{\rm eq}\,a^2R}{6g_2(\beta)\Omega}. \tag{55}$$

$\theta \geqslant 1$ simply means that there is more than enough As at nucleation to form a full ML, so that stage 2 will vanish ($p = 0$).

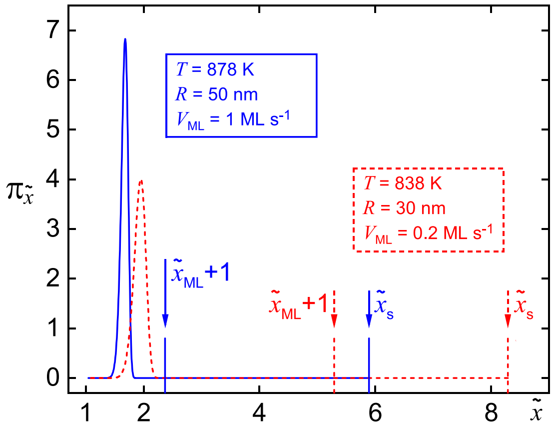

FIG. 8. Probability density of the reduced As concentration in the Ga droplet at nucleation, calculated analytically at growth temperature $T = 838$ K for a GaAs NW of radius $R = 30$ nm under input rate $V_{\rm ML} = 0.2$ ML s^{-1} (dashed red curve) and at $T = 878$ K for $R = 50$ nm, $V_{\rm ML} = 1$ ML s^{-1} (full blue curve). In both cases, concentration x_s at which As desorption balances input is larger than that insuring that one ML is available for growth (both marked by vertical arrows, using same line styles), but all nucleations effectively occur below the latter.

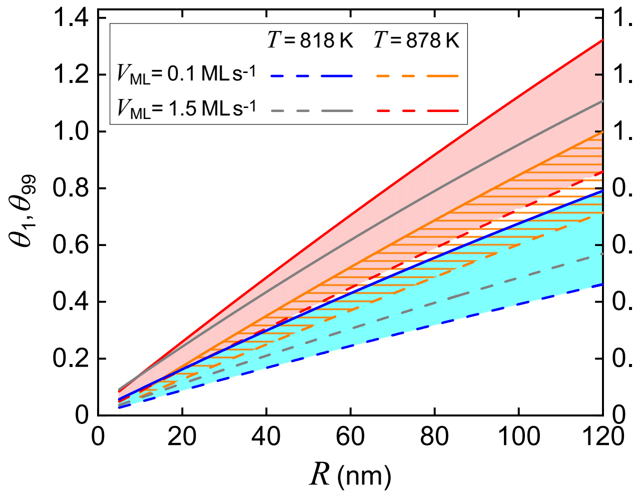

FIG. 9. Variations with NW radius of characteristic ML fractions θ_1 (dashed lines) and θ_{99} (full lines) available in the droplet at nucleation. Only 1% of nucleations occur at available fraction $\theta \leqslant \theta_1$ and 1% at $\theta \geqslant \theta_{99}$. θ_1 and θ_{99} were calculated semi-analytically for input rates of 0.1 ML s^{-1} and 1.5 ML s^{-1} at growth temperatures of 818 K (blue and gray lines, respectively) and 878 K (orange and red lines). For given growth conditions and NW radius, 98% of nucleations occur in interval $[\theta_1, \theta_{99}]$. Shading or stripes help visualize these ranges for three of our four growth conditions.

To visualize the range of ML coverages realized at stage 1, we introduce cover θ_1 such that only 1% of the nucleation events occur at a lower available ML fraction, and cover θ_{99} such that only 1% of the nucleation events occur at a higher ML fraction. In other words, 98% of the initial coverages fall between θ_1 and θ_{99} (if $\theta_{99} \geqslant 1$). Figure 9 shows the variations of θ_1 and θ_{99} with NW radius (for a fixed $\beta = 100^\circ$) at two growth temperatures and for two widely different input rates in the droplet (0.1 and 1.5 ML s^{-1}).

A more comprehensive picture appears if we map the fraction of nucleation events giving rise to a full ML in the (R, V_{ML}) plane (Fig. 10).

The general conclusion is that, at a given temperature, the domain of NW radius and As flux where an effective IML regime prevails (with the vast majority of nucleation events occurring at an available As concentration in the liquid equivalent to less than one ML) is much broader than the domain where desorption guarantees that *all* nucleations occur in this sub-ML limit (see also Fig. 7). This explains why a slow propagation of the ML step is reported in many *in situ* studies of the growth of WZ sections in GaAs NWs, despite the variety of methods, NW radius and growth conditions employed [4–7].

It may seem surprising that the effective IML domain shrinks with increasing temperature (Fig. 10), whereas the opposite occurs for the strict IML domain (Fig. 7). In the latter case, the boundary is set by the balance between As input and desorption (Sec. VI A). When T increases, desorption increases and a lower As concentration suffices to balance a given input, which means that the IML condition is easier to achieve. On the contrary, the effective IML regime requires that most nucleations occur in the sub-ML concentration range. At given As concentration, the nucleation rate decreases with increasing T, since the decrease of the chemical potential more than offsets the easier thermal activation [17]. Hence, nucleations tend to occur at higher As concentration, making the sub-ML regime less likely.

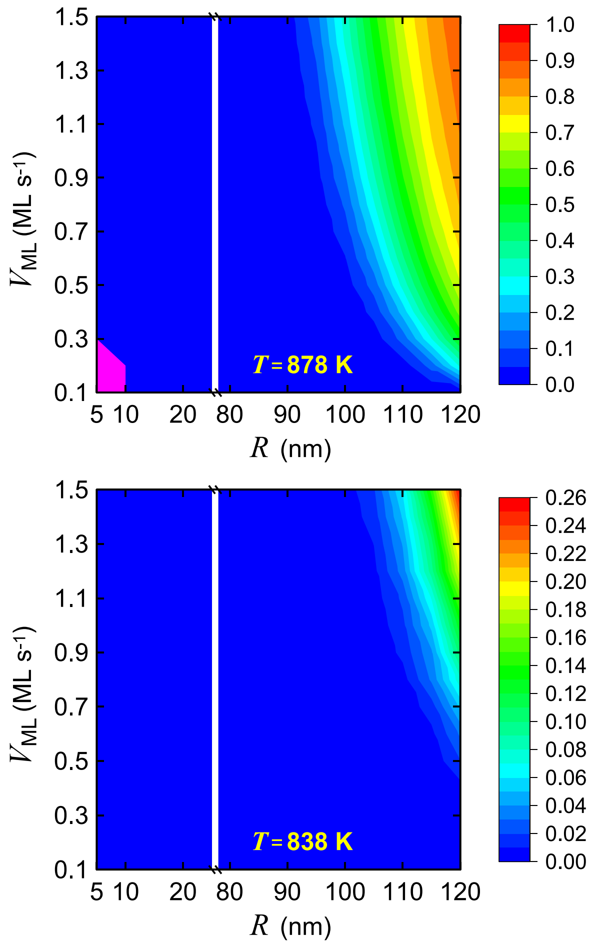

FIG. 10. Maps of the fractions of nucleation events giving rise to the formation of a complete ML at stage 1, for $T = 838$ K and $T = 878$ K. Data are not plotted in the range $R \leqslant 25 \leqslant 78$ nm, where the fractions remain less than 10^{-5}. The purple domain at the lower-left corner of the top map corresponds to critical nuclei too large to be accommodated on the NW top facet.

Since these calculations confirm that nucleation may occur at low As concentration (Figs. 8 and 9), we must examine a possible limitation to the use of Eq. (9). In nanosize systems, the number of particles may indeed be so small that the very formation of a cluster of the new phase can deplete the mother phase enough to diminish significantly the chemical potential [45] (see other references in Ref. [8]). Using Eq. (9), with a nucleation barrier fixed by the concentration just before nucleation, might then be inaccurate. Since nucleation occurs in a narrow x range (Figs. 8, 9, and 11), the number N_n of As atoms in the liquid at nucleation scales approximately as R^3 whereas the number N_c of As atoms in the critical nucleus (as calculated in Sec. III B) is independent of R. Hence, any effect of depletion on nucleation itself would decrease quickly as R increases. To find out if this may become significant at small radius, we evaluate the ratio N_c/N_n. For $R = 10$ nm, we find ratios in the ranges 0.025–0.05 at $T = 818$ K and

0.04–0.15 at $T = 878$ K (depending on As input). It is only for our narrowest NWs ($R = 5$ nm) that the ratio may become sizable (0.17–0.36 at $T = 818$ K and 0.3–0.5 at $T = 878$ K). However, the present work is mainly concerned with the characteristics of the proper mixed regime and with the transition between IML and mixed regimes, which only occur at much higher radii. For instance, at $R = 50$ nm (where the IML regime still prevails; see Fig. 10), the ratio remains well below 10^{-3}.

VII. QUASIDETERMINISTIC GROWTH IN THE EFFECTIVE INCOMPLETE MONOLAYER REGIME

We showed in Sec. II A that strict IML regime and absence of desorption [conditions (A1) and (A2)] are necessary for a fully deterministic growth regime, where all intervals between ML completions last exactly the same time τ_c. We now examine if the effective IML regime, which we have shown to occur over a wide range of growth parameters (Sec. VI B, Figs. 7–10), could result in a quasideterministic growth regime, defined by a narrow distribution of ML cycle times τ_c.

Figure 11 shows the variations with NW radius of the average $\langle \tilde{x}_n \rangle$ and standard deviation $\sigma_{\tilde{x}_n}$ of the concentration $\tilde{x}_n$ at nucleation [Figs. 11(a) and 11(b), upper panels] and of the average and standard deviation of the ML cycle time τ_c, both normalized by input rate [Figs. 11(a) and 11(b), lower panels], for low and high As input rates. Arsenic desorption is moderate at $T = 838$ K [Fig. 11(b)] and strong at $T = 878$ K [Fig. 11(a)].

Before turning to statistics, let us briefly discuss how $\langle \tilde{x}_n \rangle$ varies with the growth parameters. $\langle \tilde{x}_n \rangle$ depends only weakly on R and V_{ML}, albeit systematically. This can be understood as follows: At a given temperature, the nucleation probability per unit time [Eqs. (8) and (11)] increases with $\tilde{x}$, which itself increases over waiting time in a given fashion (set by input and desorption) at a given radius [Eq. (3) and Fig. 3]. If the waiting time starts from $\tilde{x} \simeq 1$ (IML or effective IML regime), the total nucleation probability up to any concentration $\tilde{x}$ thus decreases when V_{ML} increases, since the liquid spends a shorter time in the range up to $\tilde{x}$. Nucleation will thus occur on average at a higher concentration: at fixed R, $\langle \tilde{x}_n \rangle$ increases with V_{ML}. Conversely, at fixed V_{ML}, since the atom input rate scales with R^2, the rate of increase of $\tilde{x}$ during w scales with R^{-1} when desorption is low and anyway decreases when R increases. Hence, the larger R, the longer the liquid experiences the range up to $\tilde{x}$. When R increases, the total nucleation probability up to any concentration thus increases and consequently $\langle \tilde{x}_n \rangle$ decreases. Finally, at given radius and input, when temperature increases, desorption increases and the time spent to reach a certain concentration $\tilde{x}$ becomes longer. The probability that nucleation occurs below $\tilde{x}$ thus increases, which implies that $\langle \tilde{x}_n \rangle$ decreases when T increases. This explains all trends in the variations of $\langle \tilde{x}_n \rangle$ with growth parameters observed in Fig. 11.

Let us now consider the variations with growth conditions of the average $\langle \tau_c \rangle$ and standard deviation of the ML cycle time [Figs. 11(a) and 11(b), lower panels]. Apart from a strong increase at low NW radius due to the Kelvin effect, $\langle \tau_c \rangle$ depends very weakly on R for given V_{ML} and T. In absence of desorption, $\langle \tau_c \rangle V_{\mathrm{ML}}$ would equal 1. Hence, the increase of $\langle \tau_c \rangle V_{\mathrm{ML}}$ when V_{ML} decreases (at fixed R) must relate to the longer time over which desorption operates which more than balances the exploration of larger concentrations by the liquid at larger V_{ML} discussed above. Indeed, both this increase and the Kelvin effect are more marked at higher temperature.

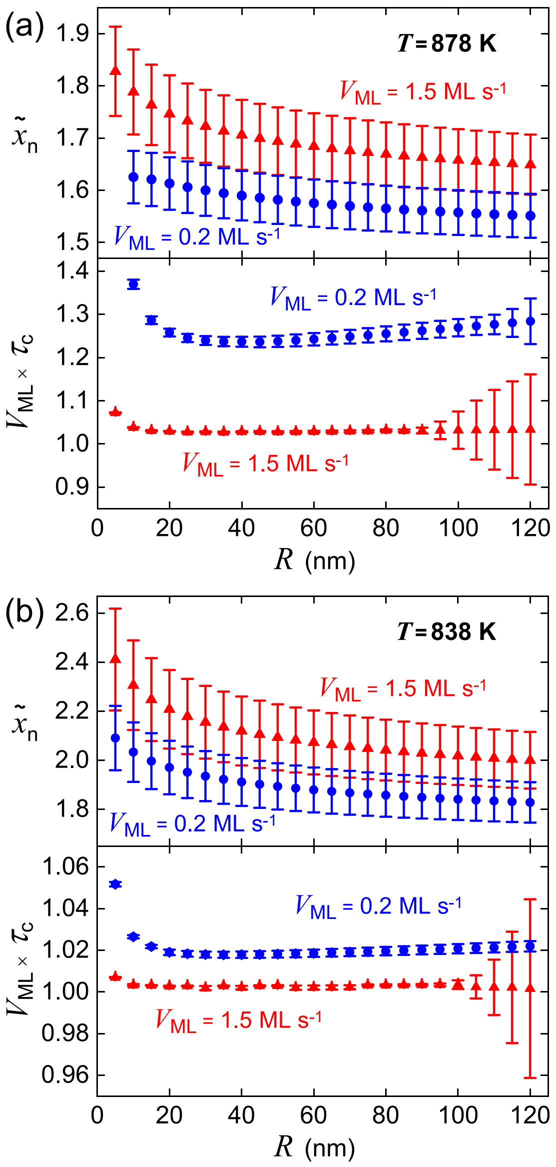

FIG. 11. Variation with NW radius of the averages (symbols) and dispersions (bars) of the concentration $\tilde{x}_n$ at nucleation [(a), (b), upper panels] and of the ML cycle time τ_c normalized by As input rate V_{ML} [(a), (b), lower panels], for low and high input rates, at (a) $T = 878$ K and (b) $T = 838$ K. The bars correspond to one standard deviation on each side of the averages for both quantities (the distributions of which are asymmetric; see Figs. 5 and 8).

Remarkably, the standard deviation of $\tau_c V_{\mathrm{ML}}$ remains small except at large NW radii and high input rate, and then the effect is stronger at higher temperature. This relatively high dispersion correlates with the domain of growth conditions where the effective IML regime breaks down (upper corners of maps of Fig. 10) and can be explained as in Sec. II A: for the sizable fraction of nucleations then occurring with enough As to complete a ML, τ_c reduces to random waiting time w [Fig. 1(b)].

What remains to be explained is the low dispersion of τ_c in the other conditions (where the effective IML regime prevails), even at temperatures where significant desorption is expected [Fig. 11(a)], in apparent contradiction with the conclusion of Sec. II A that self-regulation requires low desorption in addition to the IML regime. To understand this, we consider the variation of concentration in absence of nucleation during waiting time [Eq. (3)], starting from $\tilde{x} \simeq 1$ (effective IML regime). This is first illustrated schematically in Fig. 3. If nucleation occurs in a range close to $\tilde{x}_s$ (label r3), then w is broadly distributed but p is not (all fractional MLs have nearly the same size, set by $\tilde{x}_s$), and the τ_c distribution will indeed be broad. If, however, nucleation occurs in a range (label r1) where $\tilde{x}$ increases quasilinearly with time, the arguments developed in Sec. II A for joint weak desorption and IML regime still hold and the τ_c distribution will be narrow. Then, although the increase of $\tilde{x}$ with time may become strongly sublinear, especially at high temperature, the concentrations where this would happen are never actually reached. Note that, from Eq. (3), whatever the desorption constant $D \leqslant V$, $\tilde{x} \simeq 1 + (V - D)w$ for $w \ll (DV)^{-1/2}/2$: initially, $\tilde{x}$ always increases quasilinearly, albeit at a rate less than V. Finally, if nucleation occurs in a range r2 where strong desorption makes $\tilde{x}$ increase nonlinearly with time, the τ_c distribution can still be narrow, provided the nucleation composition range is narrow, since $\tilde{x}$ increases deterministically from $\tilde{x} \simeq 1$ at beginning of waiting time while p is, as usual, set by the nucleation composition. In summary, nucleation in ranges such as r1 or r2 should produce quasideterministic growth.

Actual calculations are illustrated in Fig. 12, where colored boxes show, for growth conditions spanning wide ranges of NW radii and input and desorption rates, the domains of concentration and waiting time over which most nucleation events occur (each box is centered at $\langle\tilde{x}_n\rangle$ and extends over $\pm 2\sigma_{\tilde{x}_n}$). At $T = 838$ K, $\tilde{x}$ appears to increase quasilinearly with w and the effective IML regime is realized except for $R = 120$ nm, $V_{\rm ML} = 1.5$ ML s^{-1}: about a quarter of nucleation events then produce complete MLs (Fig. 10). Accordingly, the τ_c distribution is narrow, except in this case. At $T = 878$ K, the effective IML regime is not realized for $R = 120$ nm and this makes the τ_c distribution fairly broad, at both low and high input (Fig. 11). For $R = 10$ nm, the effective IML regime is realized for both inputs and the τ_c distribution is narrow, which can be attributed to the quasilinear increase of $\tilde{x}$ with w or narrow nucleation range seen in Fig. 12 (cases r1 or r2 of Fig. 3).

In summary, the system may deviate from quasideterministic growth (defined by a narrow ML cycle time distribution) for growth conditions such that the effective IML regime is not realized. However, this is expected to occur only at high growth temperature and large NW radius. Strong desorption, which could also in principle inhibit quasideterministic growth, does not seem to be deleterious in itself since nucleation tends to occur before the As concentration reaches levels where its increase with time becomes noticeably sublinear.

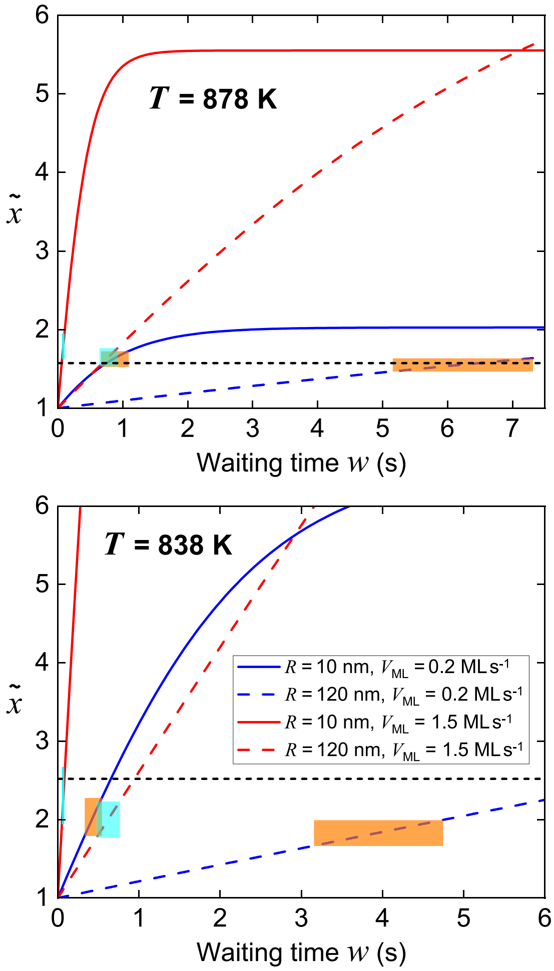

FIG. 12. Variation over waiting time of the reduced As concentration in the liquid for small and large NW radii and input rates, at two temperatures. The colored boxes show, for each set of growth conditions (line styles apply to both temperatures), the domains of concentration and waiting time over which most nucleation events occur. Vertically, each box is centered at $\langle\tilde{x}_n\rangle$ and extends over $\pm 2\sigma_{\tilde{x}_n}$. The dashed horizontal lines give the values of $\tilde{x}_{\rm ML} + 1$ for $R =$ 120 nm (the values for $R = 10$ nm are out of the $\tilde{x}$ range displayed).

VIII. SUMMARY AND CONCLUSIONS

We have studied theoretically the various regimes of formation of ML sequences during VLS growth of semiconductor NWs, when all material is provided by the liquid nanodroplet. If at nucleation this one does not contain enough of at least one element to build an entire ML, growth starts with the quasi-instantaneous crystallization of an incomplete ML (consuming all atoms in excess of equilibrium), which then propagates by using the steady vapor input into the liquid. Next ML nucleates after a random waiting time during which the droplet refills.

We extended our previous study of the proper *incomplete monolayer (IML) regime*, where this occurs for each ML and should produce a fixed ML cycle time at low growth temperature, to the *mixed regime*, where fractional or full MLs may form, depending on the nucleation event. The statistics of all characteristic times (propagation, waiting, and ML cycle times) can be obtained from the probability density of the concentration at nucleation. These quantities were calculated semi-analytically, without resorting to growth simulations, in the most general case of the mixed regime at arbitrary temperature, with due inclusion of desorption from the liquid and small size effects. This made possible a broad discussion of the statistics of NW growth at the ML level.

Whereas the conditions for the strict IML regime are fairly restrictive, an *effective IML regime*, whereby a huge fraction of nucleations produce incomplete MLs, may prevail over a wide range of NW or droplet geometry and growth conditions, with complete MLs becoming frequent only at large NW radius, input rate, and temperature. This is key in explaining that the *in situ* studies of VLS-grown III-V or II-VI NWs that detail the development of single MLs when the solid-droplet interface is nontruncated, all report a nonzero propagation time for each ML (although, except in our own [5,8], no mention is made of a fast stage 1 preceding a slower stage 2) [4,6,9,34,46]. This strongly suggests a prevalence of the IML regime, be it strict or effective, i.e., a shortage of one element at nucleation. The quasi-instantaneous growth of a substantial ML fraction (stage 1) in our experiments and the very fast growth of a full ML in the case of truncated interfaces seem to rule out another possible explanation, a propagation limited by transport of material to the step. Even though some experiments relate to other NW or catalyst materials, our quantitative results for self-catalyzed GaAs NWs strongly suggest that the *a priori* surprising absence of the proper mixed regime stems in particular from the relatively small radii (apparently below 30 nm) of the NWs selected in the experimental studies.

Even more important is our demonstration that, in this easily achievable effective IML regime (predicted to prevail up to very large NW radii and high growth temperature), growth tends to become quasideterministic, with a very narrow distribution of ML cycle times. We attribute this remarkable property to the occurrence of most nucleations in a range where the concentration of the scarce element in the liquid increases quasilinearly with time (without strong desorption-induced nonlinearity), so that the propagation time compensates the fluctuations of the waiting time induced by the intrinsically random occurrence of the nucleation events, as in the proper IML regime.

Quasideterministic growth is very promising for a precise control of NW structures. It could for instance lead to highly uniform arrays of NWs of a single material. Apart from maintaining constant NW radius and droplet contact angle, one would then have to take into account desorption and the variation with time of the input into the droplet along some pathways. Indeed, surface diffusion of NW species or their re-emission by the environment depend on NW height, albeit in deterministic ways for which calculations do exist [32,42,47–49]. One may now also hope to control the individual segments of axial heterostructures at the ML level simply via growth duration, but this is more complex. Standard compositional structures require shifts between different materials, with possibly different statistics, and involve transient regimes. Crystal phase heterostructures of a single material eschew this problem but present an alternative difficulty. In the best studied case of the III-V compounds, each crystal structure has its own solid-liquid interface morphology [4,5,7]. Whereas the WZ MLs exhibit the planar interface considered in the present work, the formation of ZB MLs entails an oscillating truncation. The slow completion of a fractional ML from the liquid (stage 2) is then replaced by a quick completion using material transferred from the solid NW stem, causing a sudden deepening of the truncation followed by a slow refill from the liquid [19]. This will alter the statistics. We intend to extend our theoretical investigations to this case, in which one nevertheless also expects some self-regulation (small fractional MLs require a longer truncation refill).

Our calculations are particularly relevant to III-V compounds, where the concentration of the volatile group V species in the liquid is very low, and for which the three growth stages are observed by *in situ* TEM. This lead us to investigate self-catalyzed GaAs NWs in detail. However, what decides between the quick growth of either a fractional or a full ML is not the absolute number of NW atoms in the liquid at nucleation but the amount available in excess of liquid-solid equilibrium. During VLS growth of elementary semiconductors, even though the catalyst typically contains several tens of percent of NW element, the equilibrium concentration being also high, the amount available may easily be less than a ML. This is confirmed both experimentally by the observation by *in situ* TEM of a truncated interface [3] and by calculation. For instance, using available thermodynamic data [50], we find that, for Au-catalyzed Si NWs in the growth temperature range 673–873 K, a supersaturation of, e.g., 30 meV/atom requires a Si concentration of 0.017 to 0.024 above equilibrium. Then, for $\beta = 90^\circ$, any nucleation occurring below this value will produce an incomplete ML for NW radii below 15-20 nm.

Even in a system with well-known thermodynamic properties, such as self-catalyzed GaAs NWs, our fully quantitative calculations require values of the nucleation rate parameters, which are practically impossible to calculate. We used numbers from our previous joint experimental and theoretical study of such NWs, according to which a whole range of parameter couples is however admissible [8]. Although we do not expect the broad conclusions of our study to be altered, the specific figures depend on the parameters chosen. Conversely, an experimental determination of the fraction of incomplete MLs at nucleation as a function of NW radius, input or temperature and a comparison with calculated maps such as those of Fig. 10 would allow us to lift this indeterminacy.

Finally, even though the present work focused on the VLS growth of NWs, we speculate that similar self-regulation mechanisms might operate also in the cases of other growth modes (such as vapor-solid-solid or catalyst-free growth) and of other nanosize systems, where the mother phase might constitute a reservoir of species (e.g., adatoms on a small crystal facet) readily available for growth after nucleation but possibly insufficient for building a whole ML (or appropriate growth unit).

ACKNOWLEDGMENTS

The author acknowledges fruitful discussions with his colleagues J.-C. Harmand, F. Panciera, F. Oehler, G. Patriarche (C2N) and V. G. Dubrovskii (Saint Petersburg State University).

[1] F. M. Ross, J. Tersoff, and M. C. Reuter, Sawtooth faceting in silicon nanowires, Phys. Rev. Lett. **95**, 146104 (2005).

[2] A. D. Gamalski, C. Ducati, and S. Hofmann, Cyclic supersaturation and triple phase boundary dynamics in germanium nanowire growth, J. Phys. Chem. C **115**, 4413 (2011).

[3] C.-Y. Wen, J. Tersoff, K. Hillerich, M. C. Reuter, J. H. Park, S. Kodambaka, E. A. Stach, and F. M. Ross, Periodically changing morphology of the growth interface in Si, Ge, and GaP nanowires, Phys. Rev. Lett. **107**, 025503 (2011).

[4] D. Jacobsson, F. Panciera, J. Tersoff, M. C. Reuter, S. Lehmann, S. Hofmann, K. A. Dick, and F. M. Ross, Interface dynamics and crystal phase switching in GaAs nanowires, Nature (London) **531**, 317 (2016).

[5] J.-C. Harmand, G. Patriarche, F. Glas, F. Panciera, I. Florea, J.-L. Maurice, L. Travers, and Y. Ollivier, Atomic step flow on a nanofacet, Phys. Rev. Lett. **121**, 166101 (2018).

[6] C. B. Maliakkal, E. K. Mårtensson, M. U. Tornberg, D. Jacobsson, A. R. Persson, J. Johansson, L. R. Wallenberg, and K. A. Dick, Independent control of nucleation and layer growth in nanowires, ACS Nano **14**, 3868 (2020).

[7] F. Panciera, Z. Baraissov, G. Patriarche, V. G. Dubrovskii, F. Glas, L. Travers, U. Mirsaidov, and J.-C. Harmand, Phase selection in self-catalysed GaAs nanowires, Nano Lett. **20**, 1669 (2020).

[8] F. Glas, F. Panciera, and J.-C. Harmand, Statistics of nucleation and growth of single monolayers in nanowires: Towards a deterministic regime, Phys. Status Solidi RRL **16**, 2100647 (2022).

[9] E. Bellet-Amalric, F. Panciera, G. Patriarche, L. Travers, M. den Hertog, J.-C. Harmand, F. Glas, and J. Cibert, Regulated dynamics with two-monolayer steps in vapor-solid-solid growth of nanowires, ACS Nano **16**, 4397 (2022).

[10] V. G. Dubrovskii, N. V. Sibirev, G. E. Cirlin, J. C. Harmand, and V. M. Ustinov, Theoretical analysis of the vapor-liquid-solid mechanism of nanowire growth during molecular beam epitaxy, Phys. Rev. E **73**, 021603 (2006).

[11] D. Kashchiev, Dependence of the growth rate of nanowires on the nanowire diameter, Cryst. Growth Des. **6**, 1154 (2006).

[12] J. Johansson, L. S. Karlsson, C. P. T. Svensson, T. Mårtensson, B. A. Wacaser, K. Deppert, L. Samuelson, and W. Seifert, Structural properties of ⟨111⟩ B-oriented III-V nanowires, Nat. Mater. **5**, 574 (2006).

[13] F. Glas, J. C. Harmand, and G. Patriarche, Why does wurtzite form in nanowires of III-V zinc blende semiconductors? Phys. Rev. Lett. **99**, 146101 (2007).

[14] V. G. Dubrovskii and F. Glas, Vapor-liquid-solid growth of semiconductor nanowires, in *Fundamental Properties of Semiconductor Nanowires*, edited by N. Fukata and R. Rurali (Springer, Singapore, 2021), pp. 3–107.

[15] F. Glas, Chemical potentials for Au-assisted vapor-liquid-solid growth of III-V nanowires, J. Appl. Phys. **108**, 073506 (2010).

[16] F. Glas, J.-C. Harmand, and G. Patriarche, Nucleation antibunching in catalyst-assisted nanowire growth, Phys. Rev. Lett. **104**, 135501 (2010).

[17] F. Glas, M. R. Ramdani, G. Patriarche, and J.-C. Harmand, Predictive modeling of self-catalyzed III-V nanowire growth, Phys. Rev. B **88**, 195304 (2013).

[18] S. H. Oh, M. F. Chisholm, Y. Kauffmann, W. D. Kaplan, W. Luo, M. Rühle, and C. Scheu, Oscillatory mass transport in vapor-liquid-solid growth of sapphire nanowires, Science **330**, 489 (2010).

[19] V. G. Dubrovskii and F. Glas, Oscillations of truncation in vapor-liquid-solid nanowires (unpublished).

[20] F. Glas, Statistics of sub-Poissonian nucleation in a nanophase, Phys. Rev. B **90**, 125406 (2014).

[21] F. Glas and V. G. Dubrovskii, Energetics and kinetics of monolayer formation in vapor-liquid-solid nanowire growth, Phys. Rev. Mater. **4**, 083401 (2020).

[22] S. Kodambaka, J. Tersoff, M. C. Reuter, and F. M. Ross, Germanium nanowire growth below the eutectic temperature, Science **316**, 729 (2007).

[23] F. Dhalluin, P. J. Desré, M. I. den Hertog, J.-L. Rouvière, P. Ferret, P. Gentile, and T. Baron, Critical condition for growth of silicon nanowires, J. Appl. Phys. **102**, 094906 (2007).

[24] G. Priante, G. Patriarche, F. Oehler, F. Glas, and J.-C. Harmand, Abrupt GaP/GaAs interfaces in self-catalyzed nanowires, Nano Lett. **15**, 6036 (2015).

[25] D. Spirkoska, J. Arbiol, A. Gustafsson, S. Conesa-Boj, F. Glas, I. Zardo, M. Heigoldt, M. H. Gass, A. L. Bleloch, S. Estrade, M. Kaniber, J. Rossler, F. Peiro, J. R. Morante, G. Abstreiter, L. Samuelson, and A. Fontcuberta i Morral, Structural and optical properties of high quality zinc-blende/wurtzite GaAs nanowire heterostructures, Phys. Rev. B **80**, 245325 (2009).

[26] K. A. Dick, P. Caroff, J. Bolinsson, M. E. Messing, J. Johansson, K. Deppert, L. R. Wallenberg, and L. Samuelson, Control of III-V nanowire crystal structure by growth parameter tuning, Semicond. Sci. Technol. **25**, 024009 (2010).

[27] M. Bouwes Bavinck, K. D. Jöns, M. Zieliński, G. Patriarche, J.-C. Harmand, N. Akopian, and V. Zwiller, Photon cascade from a single crystal phase nanowire quantum dot, Nano Lett. **16**, 1081 (2016).

[28] M. Taherkhani, M. Willatzen, E. V. Denning, I. E. Protsenko, and N. Gregersen, High-fidelity optical quantum gates based on type-II double quantum dots in a nanowire, Phys. Rev. B **99**, 165305 (2019).

[29] V. G. Dubrovskii, Refinement of nucleation theory for vapor-liquid-solid nanowires, Cryst. Growth Des. **17**, 2589 (2017).

[30] A. H. Persad and C. A. Ward, Expressions for the evaporation and condensation coefficients in the Hertz-Knudsen relation, Chem. Rev. (Washington, DC, US) **116**, 7727 (2016).

[31] I. Ansara, C. Chatillon, H. L. Lukas, T. Nishizawa, H. Ohtani, K. Ishida, M. Hillert, B. Sundman, B. B. Argent, A. Watson, T. G. Chart, and T. Anderson, A binary database for III-V compound semiconductor systems, CALPHAD: Comput. Coupling Phase Diagrams Thermochem. **18**, 177 (1994).

[32] V. G. Dubrovskii, N. V. Sibirev, J. C. Harmand, and F. Glas, Growth kinetics and crystal structure of semiconductor nanowires, Phys. Rev. B **78**, 235301 (2008).

[33] I. N. Markov, *Crystal Growth for Beginners* (World Scientific, Singapore, 2003).

[34] M. Marnauza, M. Tornberg, E. K. Mårtensson, D. Jacobsson, and K. A. Dick, In situ observations of size effects in GaAs nanowire growth, Nanoscale Horiz. **8**, 291 (2023).

[35] C.-Y. Yeh, Z. W. Lu, S. Froyen, and A. Zunger, Zinc-blende-wurtzite polytypism in semiconductors, Phys. Rev. B **46**, 10086 (1992).

[36] S. M. Ross, *Introduction to Probability Models*, 11th ed. (Academic Press, Oxford, 2014).

[37] M. Abramowitz and I. A. Stegun, *Handbook of Mathematical Functions* (Dover, New York, 1970).

[38] W. Gautschi, Efficient computation of the complex error function, SIAM J. Numer. Anal. **7**, 187 (1970).

[39] R. J. Wells, Rapid approximation to the Voigt/Faddeeva function and its derivatives, J. Quant. Spectrosc. Radiat. Transfer **62**, 29 (1999).

[40] IMSL libraries, https://www.imsl.com/

[41] I. Mezö and Á. Baricz, On the generalization of the Lambert W function, Trans. Am. Math. Soc. **369**, 7917 (2017).

[42] A. Pishchagin, F. Glas, G. Patriarche, A. Cattoni, J.-C. Harmand, and F. Oehler, Dynamics of droplet consumption in vapor-liquid-solid III-V nanowire growth, Cryst. Growth Des. **21**, 4647 (2021).

[43] F. Glas, Vapor fluxes on the apical droplet during nanowire growth by molecular beam epitaxy, Phys. Status Solidi B **247**, 254 (2010).

[44] F. Glas, Erratum to "Vapor fluxes on the apical droplet during nanowire growth by molecular beam epitaxy," Phys. Status Solidi B **252**, 1897 (2015).

[45] A. I. Rusanov, The thermodynamics of processes of new-phase formation, Russ. Chem. Rev. **33**, 385 (1964).

[46] C. B. Maliakkal, M. Tornberg, D. Jacobsson, S. Lehmann, and K. A. Dick, Vapor-solid-solid growth dynamics in GaAs nanowires, Nanoscale Adv. **3**, 5928 (2021).

[47] V. Ruth and J. P. Hirth, Kinetics of diffusion-controlled whisker growth, J. Chem. Phys. **41**, 3139 (1964).

[48] P. Krogstrup, H. I. Jørgensen, E. Johnson, M. H. Madsen, C. B. Sørensen, A. Fontcuberta i Morral, M. Aagesen, J. Nygård, and F. Glas, Advances in the theory of III-V nanowire growth dynamics, J. Phys. D: Appl. Phys. **46**, 313001 (2013).

[49] F. Oehler, A. Cattoni, A. Scaccabarozzi, G. Patriarche, F. Glas, and J.-C. Harmand, Measuring and modeling the growth dynamics of self-catalyzed GaP nanowire arrays, Nano Lett. **18**, 701 (2018).

[50] F. G. Meng, H. S. Liu, L. B. Liu, and Z. P. Jin, Thermodynamic description of the Au-Si-Sn system, J. Alloys Compd. **431**, 292 (2007).